Draft version November 3, 2022
Typeset using LaTeX twocolumn style in AASTeX631

Salt-bearing disk candidates around high-mass young stellar objects

Adam Ginsburg [1] Brett A. McGuire [2,3] Patricio Sanhueza [4,5] Fernando Olguin [6] Luke T. Maud [7] Kei E. I. Tanaka [8,4] Yichen Zhang [9,10] Henrik Beuther [11] and Nick Indriolo [12]

[1]Department of Astronomy, University of Florida, P.O. Box 112055, Gainesville, FL, USA
[2]Department of Chemistry, Massachusetts Institute of Technology, Cambridge, MA 02139
[3]National Radio Astronomy Observatory, Charlottesville, VA 22903
[4]National Astronomical Observatory of Japan, National Institutes of Natural Sciences, 2-21-1 Osawa, Mitaka, Tokyo 181-8588, Japan
[5]Department of Astronomical Science, SOKENDAI (The Graduate University for Advanced Studies), 2-21-1 Osawa, Mitaka, Tokyo 181-8588, Japan
[6]Institute of Astronomy and Department of Physics, National Tsing Hua University, Hsinchu 30013, Taiwan
[7]ESO Headquarters, Karl-Schwarzchild-Str 2 85748 Garching, Germany
[8]Center for Astrophysics and Space Astronomy, University of Colorado Boulder, Boulder, CO 80309, USA
[9]Department of Astronomy, University of Virginia, Charlottesville, VA 22904, USA
[10]RIKEN Cluster for Pioneering Research, Wako, Saitama 351-0198, Japan
[11]Max Planck Institute for Astronomy, Königstuhl 17, 69117, Heidelberg, Germany
[12]AURA for the European Space Agency (ESA), Space Telescope Science Institute, 3700 San Martin Drive, Baltimore, MD 21218, USA

ABSTRACT

Molecular lines tracing the orbital motion of gas in a well-defined disk are valuable tools for inferring both the properties of the disk and the star it surrounds. Lines that arise only from a disk, and not also from the surrounding molecular cloud core that birthed the star or from the outflow it drives, are rare. Several such emission lines have recently been discovered in one example case, those from NaCl and KCl salt molecules. We studied a sample of 23 candidate high-mass young stellar objects (HMYSOs) in 17 high-mass star-forming regions to determine how frequently emission from these species is detected. We present 5 new detections of water, NaCl, KCl, PN, and SiS from the innermost regions around the objects, bringing the total number of known briny disk candidates to 9. Their kinematic structure is generally disk-like, though we are unable to determine whether they arise from a disk or outflow in the sources with new detections. We demonstrate that these species are spatially coincident in a few resolved cases and show that they are generally detected together, suggesting a common origin or excitation mechanism. We also show that several disks around HMYSOs clearly do not exhibit emission in these species. Salty disks are therefore neither particularly rare in high-mass disks, nor are they ubiquitous.

1. INTRODUCTION

Circumstellar accretion disks develop around forming new stars. While the presence of disks around low-mass stars has been clear for decades, we have only definitively demonstrated that accretion disks exist around high-mass young stellar objects (HYMSOs) in the last decade (e.g., Beltrán & de Wit 2016; Maud et al. 2017; Ilee et al. 2018).

One limiting factor in the detection and subsequent characterization of HYMSOs has been the lack of molecular emission lines that arise from the disk, but are not confused with or absorbed by the surrounding molecular cloud. A select few lines have recently been discovered that are uniquely produced in the disks of some HMYSOs. Emission from salt molecules has been detected in the surroundings of four stars in three star-forming regions: Orion Source I (Ginsburg et al. 2019a), G17.64+0.16 (Maud et al. 2019), and a pair in IRAS 16547-4247 (Tanaka et al. 2020) (hereafter, SrcI, G17, and I16547, respectively). Of these, SrcI and G17 are confirmed disks, while the I16547 pair remain candidates, and in all cases the salt emission comes from zones within $\lesssim$ 100 au of the central source. Each of these sources also exhibits H_2O emission from both the (candidate) disk and a slightly more extended region, and thus we dub these objects 'brinaries.'

Salts are detected in the atmospheres of AGB and post-AGB stars, giving some clues as to the physical conditions needed to produce them. Salts have been detected in CRL2688 (Highberger et al. 2003), IRAS+10216 (Cernicharo & Guelin 1987), IK Tauri, VY Canis Majoris (Milam et al. 2007; Decin et al. 2016), VX Sgr (mentioned in passing in Danilovich et al. 2021), and OH231.8+44.2 (Sánchez Contreras et al. 2022). Sánchez Contreras et al. (2022) discovered a brinary disk surrounding the post-AGB mass transfer system OH231.8+4.2, highlighting the similarity between birth and death among moderately massive stars. However, there are also some non-detections in well-surveyed sources, including the S-type AGB stars W Aql and π^1 Gru (Homan et al. 2020; Danilovich et al. 2021).

The development of line lists in the infrared, and more complete lists in the radio, has been driven in part by interest in salts as constituents of the atmospheres of hot planets, in which these species are predicted to be important components of upper cloud layers (Barton et al. 2014). There is therefore some motivation to understand where salts occur in disks and in or on dust grains.

Studies of (post)-AGB stars and models of planetary atmospheres provide some clues about the physical conditions required to produce gas-phase salts. NaCl is expected to change states (from solid to gas or vice-versa) around ∼500–600 K at planetary atmospheric pressure (i.e., 1 bar; Woitke et al. 2018). Decin et al. (2016) suggest that it comes off of grains at 100–300 K based on the detection locations in supergiant stars. These studies provide a first hint about where NaCl may come from if it precipitates out of cooling gas, though it remains unclear if the same mechanisms apply in and around YSO disks.

Motivated by the detection of salts in a few HMYSOs with ALMA in recent years, we present a first search for salt-bearing disks in the ALMA archives. In Section 2, we describe the ALMA observations we analyze. In Section 3, we describe the analysis approach (3.1.1) and detections (3.3). We discuss the chemical correlations observed in the sample and possible reasons for (non)detections in Section 4, then conclude.

2. DATA & SAMPLE SELECTION

We utilize archival and new data from several projects. We select data sets that have high angular resolution ($\lesssim 0.1''$) targeting high-mass star-forming regions. Most of the sources in our sample come from the Digging into the Interior of Hot Cores with ALMA (DIHCA; PI: Sanhueza) program, which is surveying ∼ 30 candidate disks. The main aims of the DIHCA survey are to study the interior of massive hot cores to determine whether they form high-mass stars collapsing monolithically or by fragmenting into binary (multiple) systems and to search for accretion disks around high-mass stars. The DIHCA targets were selected from the literature as regions with previous interferometric (e.g., SMA) observations and having an expected flux of >0.1 Jy at 230 GHz. All clumps follow the empirical threshold for high-mass star formation suggested by Kauffmann & Pillai (2010). We only examine a small subset of the DIHCA sample here because not all data were available as of March 2022. Because our sample is not uniformly selected, we can say little about completeness; we can only search for general trends. Nevertheless, the trends we find are interesting and suggest that observing a more uniform sample in the future would be productive.

DIHCA observations of G335, G333.23, NGC6334, IRAS16562, G34.43mm1, G29.96, and G351.77 were obtained during July 2019, and observations of G5.89, G11.92, IRAS18089, and W33A were taken both in September 2017 and July 2019. The observations were reduced using CASA (v5.4.0-70; McMullin et al. 2007). The data were then phase self-calibrated in three steps with decreasing solution intervals and the continuum subtracted following the procedure of Olguin et al. (2021). Dirty cubes were produced with a Briggs weighting robust parameter of 0.5 using the CASA `tclean` task. We use dirty image cubes for expediency, so it is possible significant improved images of these objects could be obtained, though we note that the targeted lines are generally faint and would not be affected by cleaning with typical clean parameters.

We use the SrcI data from Ginsburg et al. (2018, 2019a). We use G17 data from Maud et al. (2019). We use G351.77 data from both DIHCA and Beuther et al. (2019). We use I16547 data from both DIHCA and Tanaka et al. (2020). For each of these data sets, we refer the reader to the cited papers for the data reduction description. We include summary statistics of these observations in Table 1. We give additional details about the physical resolution, distance to the targets, and the line used as a velocity guide (see §3.1) in Table 1.

Finally, we use proprietary data toward Sh 255-IR SMA1 (hereafter S255IR) from project 2019.1.00492.S (PI Ginsburg). We use the archive-produced data products, which were cleaned with the ALMA pipeline, and imaged them with CASA 6.4.3.4. The images were cleaned to a depth of 10 mJy using Briggs robust=0 weighting.

3. RESULTS AND ANALYSIS

We search for lines of NaCl, KCl, H_2O, SiS, and H30α in each of the target pointings (see Table 2). Since each target was selected for having a high luminosity or a strong HMYSO disk candidate beforehand, we used the literature identification of existing sources as our start-

Table 1. Observation Summary

Field	Source Name	$\theta_{\rm maj}$	$\theta_{\rm maj}$	$\theta_{\rm min}$	PA	σ	$f(>5\sigma)$	$N_{\rm beams}$	$\sigma_{\rm avg}$	v ref. line	Distance
		AU	$''$	$''$	$^\circ$	K			K		kpc
Orion	SrcI	20	0.050	0.039	72.7	19.3	0.05	43	2.9	NaCl J=18-17 v=0	0.4
S255IR	SMA1	40	0.036	0.027	5.6	46.9	0.04	19	10.6	no clear disk	1.6^k
G351.77	mm12	50	0.027	0.022	-89.3	6.0	0.08	24	1.2	H_2O	2.2^c
G351.77	mm2	50	0.027	0.022	-89.3	6.0	0.05	21	1.3	H_2O	2.2^c
G351.77	mm1	50	0.027	0.022	-89.3	6.0	0.14	41	0.9	H_2O	2.2^c
G17	G17	50	0.038	0.022	44.4	10.0	0.01	75	1.2	H_2O	2.2^c
NGC6334I	mm1d	50	0.074	0.041	62.8	19.6	0.10	20	4.3	H_2O	1.3^d
NGC6334I	mm1b	50	0.074	0.041	62.8	19.6	0.23	27	3.7	H_2O	1.3^d
NGC6334I	mm2b	50	0.074	0.041	62.8	19.6	0.07	7	7.0	H_2O	1.3^d
NGC6334IN	SMA1b/d	50	0.074	0.042	63.4	17.5	0.16	278	1.0	H_2O	1.3^d
NGC6334IN	SMA6	50	0.074	0.042	63.4	17.5	0.06	22	3.7	H_2O	1.3^d
IRAS18162	GGD27	90	0.099	0.066	-89.0	6.9	0.01	36	1.1	SO 6_5-5_4	1.3^a
IRAS18089	I18089-1732	100	0.064	0.045	65.8	18.4	0.33	57	2.4	CH_3OH	2.3^f
G34.43	mm1	110	0.105	0.069	59.5	9.2	0.35	53	1.3	no clear disk	1.6^l
IRAS16562	G345.4938+01.4677	120	0.106	0.053	81.6	10.5	0.04	25	2.1	H30α	2.3^g
I16547	A	130	0.065	0.043	35.7	23.2	0.19	7	8.4	H_2O	2.9^c
I16547	B	130	0.065	0.043	35.7	23.2	0.18	5	9.5	H_2O	2.9^c
G5.89	mm15	130	0.063	0.043	66.3	19.2	0.00	85	2.1	H_2O	3.0^b
G335	ALMA1	140	0.066	0.041	47.3	20.4	0.29	118	1.9	no clear disk	3.3^i
W33A	mm1-main	170	0.103	0.067	-86.4	6.5	0.17	51	0.9	H_2O	2.6^k
G333.23	mm1	220	0.069	0.041	54.1	18.4	0.02	70	2.2	SO 6_5-5_4	5.3^h
G333.23	mm2	220	0.069	0.041	54.1	18.4	0.08	45	2.7	SO 6_5-5_4	5.3^h
G11.92	mm1	220	0.101	0.066	-86.9	6.6	0.16	103	0.7	SO 6_5-5_4	3.3^e
G29.96	submm1	530	0.099	0.071	65.0	9.6	0.22	369	0.5	no clear disk	7.4^j

Observation properties. The ‘Field’ name indicates the region of the ALMA pointing. The ‘Source Name’ is the identifier of the disk candidate examined. θ gives the beam parameters, with θ_{maj} [au] providing the physical size using the adopted distance. σ is the average noise level of the field, which is averaged down by $N_{beams}^{1/2}$ to give $\sigma_{\rm avg}$, the noise level in the stacked spectrum. $f(>5\sigma)$ is the fraction of the stacked spectrum that is above five times σ_{avg}; it is used as a diagnostic of the line crowding in the spectrum covering 219.2–220.8 GHz, which is high for complex-molecule-rich regions. The v reference line is the line used to create a velocity map to produce stacked spectra. Section 3.1.4 provides additional details. Distances come from the following sources: [a] Añez-López et al. (2020), [b] Sato et al. (2014); Fernández-López et al. (2021), [c] Beuther et al. (2017), [d] Chibueze et al. (2014), [e] Sato et al. (2014), [f] Xu et al. (2011), [g] Guzmán et al. (2020), [h] Whitaker et al. (2017), [i] Peretto et al. (2013), [j] Kalcheva et al. (2018), [k] Reid et al. (2014), [l] Kurayama et al. (2011), [m] Ilee et al. (2018),

ing point. We cut out cubes centered on the brightest continuum source in the ALMA images (except G5.89; see §B.4). We also searched fainter continuum sources, selecting small sub-regions around each of the compact continuum peaks that could plausibly contain disks. Because the source selection is based on a by-eye examination of the data over a limited field of view (in most cases, only the inner 5–10 arcseconds of the ALMA field of view was imaged), the sample presented here has unknown completeness - the conclusions we draw will therefore be only suggestive, not conclusive.

Most of our line detections come from stacked spectra of resolved disk-like objects. We describe in Section 3.1 the line stacking approach used to obtain higher signal-to-noise ratio spectra that represent average values over the candidate disk. Section 3.3 describes the detections in individual sources and shows some of the extracted images and spectra. Additional images and spectra are displayed in the appendices.

The main result is the detection of the ‘brinary’ lines toward the 9 sources (of which 3 are tentative detections) shown in Figures 1 and 2. These initial figures show moment maps of the NaCl lines as described in Section 3.1.3.

3.1. *Line stacking extraction*

From source candidate identification from the continuum data, the analysis forks down two different paths.

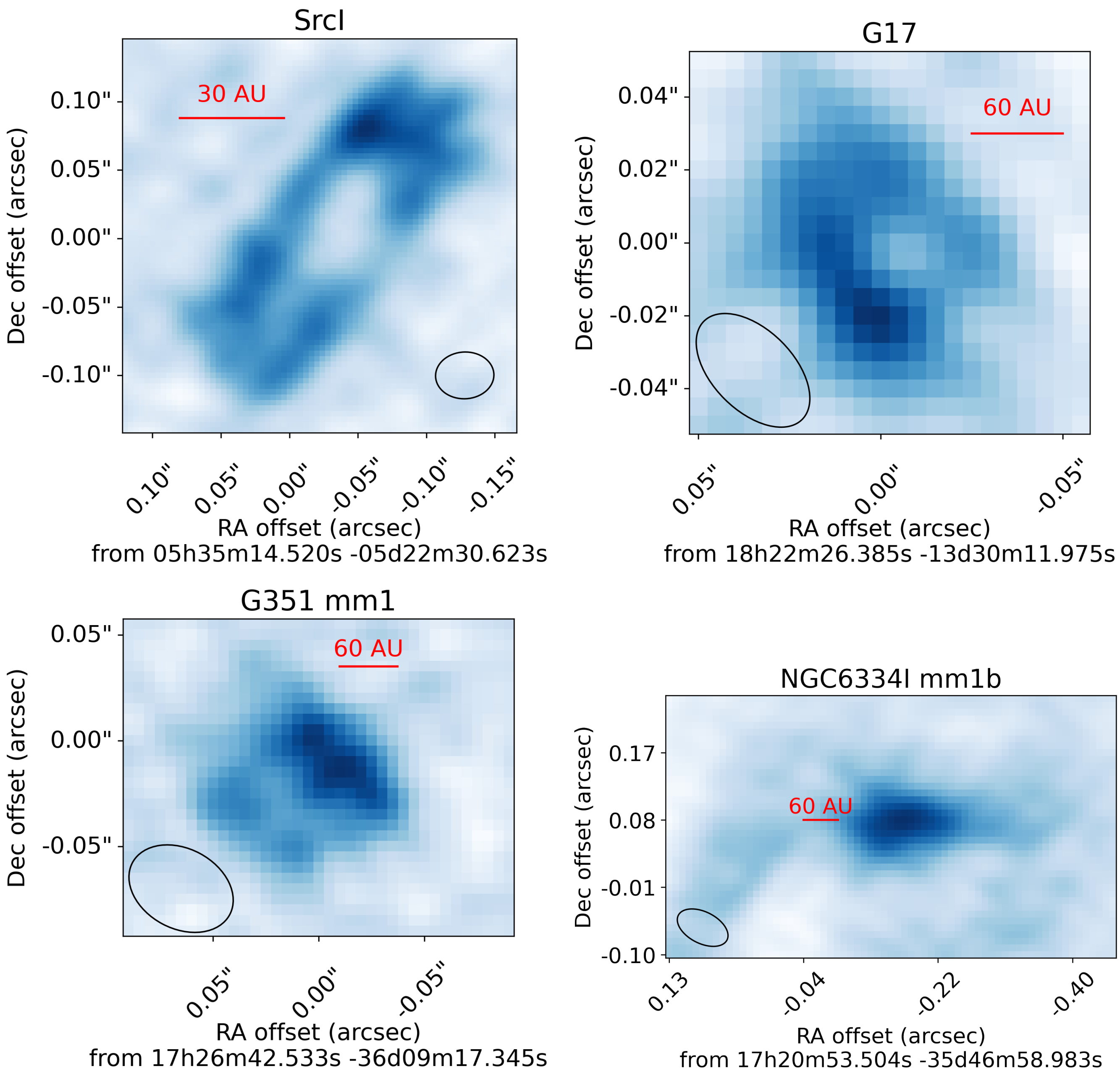

Figure 1. Moment-0 (integrated intensity) images of the resolved sources in NaCl lines. For SrcI (top-left), this is the integrated intensity of the NaCl J=18-17 v=0 line. For the remainder, G17 (top right), G351 mm1 (bottom left), and NGC 6334I mm1b (bottom right), these are the average of the J=18-17 and J=17-16 transitions of both the v=0 and v=1 states. The coordinates are given in RA/Dec offset from the central position specified under the abscissa. The scalebars show physical sizes as labeled. The ellipses in the corners show the full-width half-maximum beam ellipse.

We start by searching by eye for emission associated with the H_2O line, which is quite bright in SrcI, in §3.1.1, which we then use as a kinematic reference. If water is not detected, we use a different line as our kinematic reference as described in §3.1.2.

3.1.1. *Water-driven analysis*

If the water line is detected, we use it to create a 'velocity map' following this procedure:

1. Cut out a cube containing the region around the estimated central $v_{\rm LSR} \pm 20\,{\rm km\ s^{-1}}$ in velocity and encompassing only the candidate disk region in space.

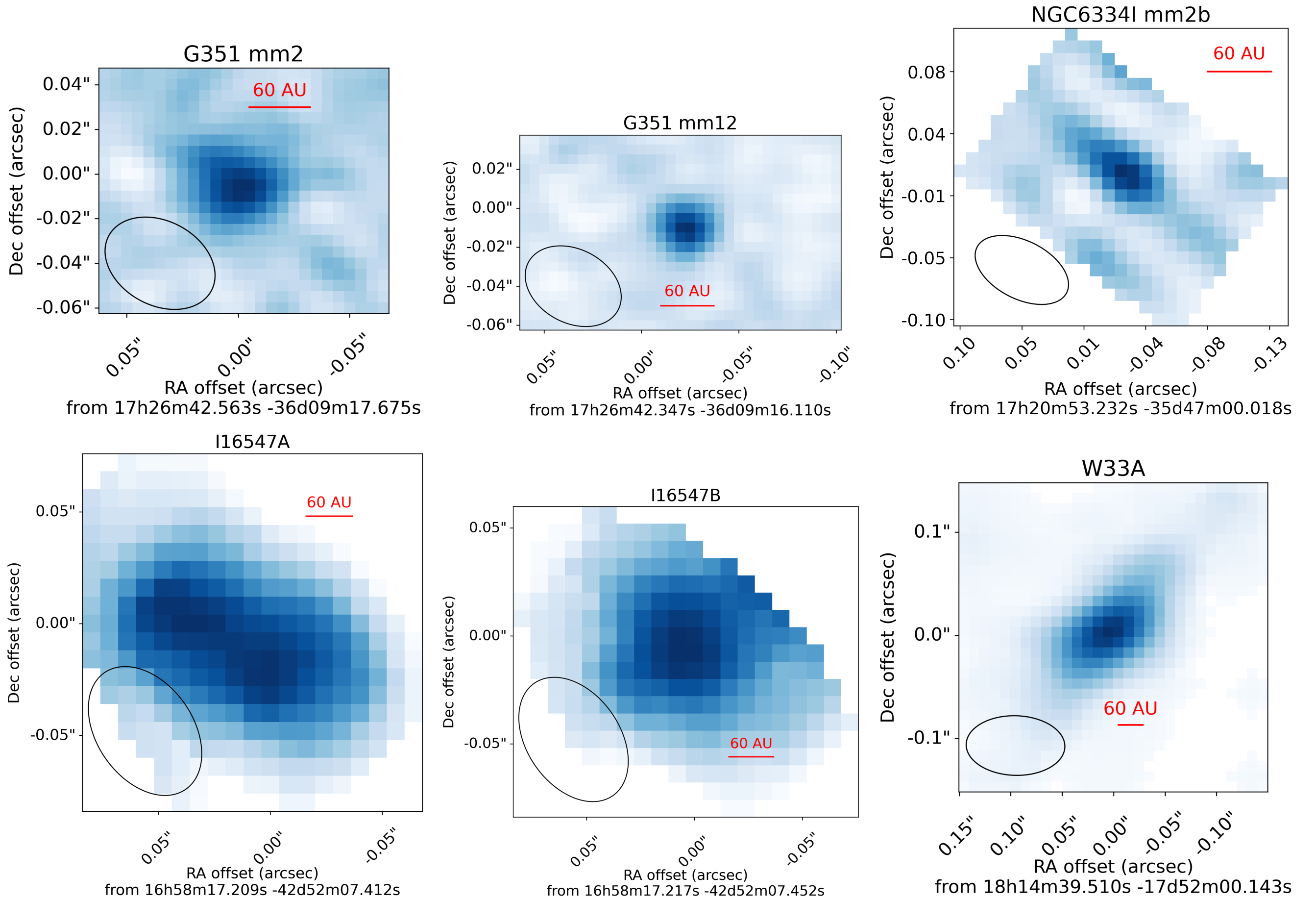

Figure 2. Integrated intensity (moment-0) images of the NaCl stacked lines toward G351mm2 (top left), G351mm12 (top middle), NGC 6334I mm2b - which is only a tentative detection (top right), I16547A (bottom left) and B (bottom center), and W33A (bottom right). These disk candidates are either unresolved or marginally resolved.

2. Create a peak intensity map of the line in that region.

3. Create a threshold mask including only the (by-eye) estimated significant emission in the peak intensity map. Use one iteration of binary erosion and three to seven iterations of binary dilation to remove isolated bright noise pixels and fill back in the mask.[1]

4. Create a volumetric threshold mask including only pixels above the estimated noise level. Then, use one iteration of binary erosion followed by one to three iterations of binary dilation to fill in the mask. As in the previous step, this step is to eliminate isolated bright pixels, but because it is in 3D, a different threshold can be adopted.

5. Create a moment-1 (intensity-weighted velocity) map of the spatially and volumetrically masked data cube.

The erosion and dilation steps are performed to exclude isolated bright pixels and to maximally include all pixels associated with source emission.

We then use the velocity map to stack the spectra obtained across the disk candidate. Each spectrum from each spatial pixel in the cube that has a measured velocity is shifted such that the line peak is moved to 0 km s^{-1}. The spectra are then averaged to produce the stacked spectrum.

This stacking process assumes that all spectra through the candidate disk will have similar peak intensity and width but different central velocities; this assumption held well in the SrcI spectrum (Ginsburg et al. 2018). We assume that the kinematics of our selected line are the same as the lines of interest; this assumption is justified by position-velocity diagrams in §3.3.2.

[1] Binary dilation refers to mathematical morphology operations in which any pixel having value False and a neighbor with the value True is set to True. Binary erosion is the inverse operation.

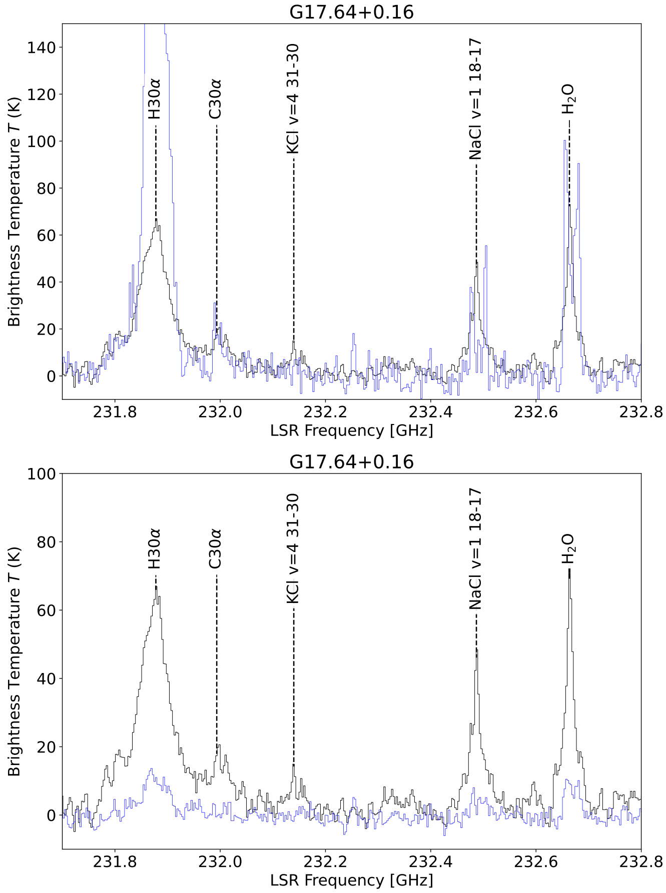

Figure 3. Demonstration of the utility of stacking analysis toward G17 in one spectral window. The black spectrum is stacked by shifting each individual spectrum to match the location of the peak intensity of the H_2O line; it is the same in both panels. The top panel shows the peak intensity spectrum taken over the same area as the stacked spectrum, and the bottom shows the mean spectrum in blue. It is clear that the stacked spectrum has clearer features and better signal-to-noise ratios than either the peak or average spectrum.

We demonstrate the advantage of this line stacking approach in Figure 3. The signal-to-noise in targeted lines is substantially increased, and faint lines appear that are otherwise missed. In the example figure, the most obvious case is KCl v=4 J=31-30, which is not apparent in either the peak intensity or average spectrum, but is strongly evident in the stacked spectrum. Those sources that are best-resolved - in our sample, G351 and G17 - show the most improvement.

We label the resulting averaged spectra with known NaCl and KCl transitions and selected other lines, including those of SiO, SiS, H_2O, H30α, and several prominent other molecules (see Table 2). We then use these plots to populate the detection table, Table 3. We regard the lines as firm detections only if they:

- Are prominent, bright, and relatively isolated (e.g., H_2O, as in Figure 4)
- Exhibit an appropriately broad linewidth (H30α is expected to have $\sigma_v \gtrsim 5$ km s^{-1} because it comes from hot plasma ($T \sim 10^4$ K), while molecular species are expected to be narrower, coming from gas at $T < 1000$ K).

For species for which we label the vibrationally excited transitions, we consider only the v=0, v=1, and v=2 levels, as higher levels are expected to be weaker if present.

There are several cases where a compelling detection of one line of a species (NaCl or KCl) is detected, but an adjacent state is not detected. For example, the J=18-17 v=1 line is detected, but the J=16-17 v=1 line is not. In these cases, we regard the detection as tentative and note it in Table 3 with an asterisk. These were cases in which the line may still be present, but may be hidden by either blending with neighboring species or absorption by a line in the surrounding core.

We report detections qualitatively rather than quantitatively because the detections are generally obvious and high signal-to-noise. When a detection is ambiguous, it is not because of high noise but because of confusion with neighboring lines (e.g., ^{41}KCl J=31-30 is confused with NaCl $v = 1$ $J = 18-17$) or absorption by non-disk material (e.g., KCl v=4 J=31-30).

3.1.2. *Water nondetection-driven analysis*

The path for water non-detections is less linear. If we are unable to clearly identify emission in the H_2O line, we search for other lines to use as the basis for stacking. We first create a simple averaged spectrum over the selected disk candidate's emitting region by examining several different lines in the cube. We then search for other plausible guiding lines, focusing on those that exhibit gradients in the direction expected given known outflows (i.e., we look at lines rotating perpendicular to outflows). We look at SiS, SO, and, when truly desperate, CH_3OH lines. If we are able to identify a reasonably disk-like line from among these lines, we use it to produce a velocity map as above (§3.1.1). If, after this search, we are still unable to find a line that traces disk-like kinematics, we remove the source from further consideration.

For both water- and non-water-driven stacking, we report the achieved noise level in Table 1.

3.1.3. *Cube stacking*

When NaCl is detected, it is generally seen in multiple transitions. The NaCl v=0 and v=1 J=18-17 and v=1 and v=2 J=17-16 transitions are present in the DIHCA observational setups and are not too badly contaminated by neighboring lines. We therefore create 'stacked' NaCl cubes by cutting out cubes centered on each of those transitions, smoothing them to a common beam, regridding them to a common spectral resolution, and then averaging the cubes. We use these stacked cubes for further analysis of the NaCl lines, producing both moment-0 images and position-velocity diagrams (except for SrcI, for which the signal-to-noise ratio in individual lines was high enough to produce moment maps without stacking). The stacked cubes have higher signal-to-noise than the individual cubes and deemphasize contaminant lines that are adjacent to the target lines, since the contaminants arise at different relative velocities for each NaCl line (for example, while the ^{41}KCl 31-30 line is 13 km s^{-1} to the red of the NaCl $v = 1$ $J = 18 - 17$ line, there is no line 13 km s^{-1} to the red of the three other NaCl lines included here). This stacking approach is not strictly necessary for use or analysis of the NaCl lines, but it aesthetically improves the resulting images and makes visual inspection and comparison more straightforward.

We created these cubes whether or not we first noted an NaCl detection in the spectrum. In cases where no detection was apparent in the stacked spetrum, we nevertheless checked the stacked NaCl cubes to see if extended emission at the expected velocity was apparent. No additional detections were obtained through this approach.

3.1.4. *COMs*

We identify the presence of complex organic molecules (COMs) in the spectrum in a very broad-strokes manner. We do not identify specific species, though we note that CH_3OH and CH_3CN are commonly detected, but instead characterize the spectra by the richness of the 'line forest.' For each observation, in the spectral range 219.2-220.8 GHz (which is COM-rich and includes the CH_3CN $J = 12 - 11$ ladder), we measure the per-pixel noise ($\sigma_{\rm cube}$) by obtaining the standard deviation over the full field of view over all pixels; this approach slightly overestimates the noise because it includes signal in the noise estimate. For image cubes that were not already continuum-subtracted, we estimate, and then subtract, the continuum by performing pixel-by-pixel sigma clipping to 3-σ, then taking the median across the spectral axis (i.e., as in Sánchez-Monge et al. 2018). Then, for each extracted region around a candidate disk, we average the spectra within that region, then determine what fraction of the spectrum exceeds five times the expected noise level, where the expected noise level is $\sigma_{\rm cube} n_{\rm beams}^{-1/2}$, where $n_{\rm beams}$ is the number of beams included in the averaging area. Note that we only search for COMs in emission; absorption by C- and O-bearing species is seen toward most sources, but is not directly associated with the candidate disk, instead, it likely comes from the surrounding envelope or molecular cloud.

Table 1 gives a summary of these statistics in addition to general properties of the data.

3.2. *Line Identification*

We briefly discuss the key lines used for identification of NaCl, KCl, PN, SiS, and SiO in this section. The summary of lines considered is in Table 2. The NaCl v=0 and v=1 J=18-17 and v=1 and v=2 J=17-16 transitions are present in the DIHCA observational setups. The $v = 1$, $J = 18-17$ line is very close to the ^{41}KCl 31-30 line, but the latter can be ruled out as a contaminant because the ^{41}KCl 29-28 is also included in the observations. In Orion SrcI, the peak intensity ratio was NaCl $v = 1$ $J = 18 - 17 \approx 5\times$ ^{41}KCl 29-28.

3.3. *Salt detections*

We detect salts in 9 sources (of which 3 are tentative) in 6 regions. Figure 1 gives an overview of those objects that are spatially resolved. In the following sections, we describe the salt-bearing sources in more detail: G17 (§3.3.1), G351 mm1, mm2, and mm12 (§3.3.2), W33A (§3.3.4), NGC6334I mm1b and mm2b (§3.3.3), and I16547 A and B (§3.3.5). The sixth region and disk, Orion SrcI, is not discussed in detail here because the same analysis was already done in Ginsburg et al. (2019a), but it is included in the discussion section below.

3.3.1. *G17*

The G17 disk is the best resolved source in our sample after SrcI (Fig 1; Maud et al. 2019). It is a confirmed Keplerian disk (Maud et al. 2019). Because of its high signal-to-noise and well-resolved structure, we investigate it in somewhat more detail than the other sources in the sample. Figure 4 shows the stacked spectrum based on the water line as described in Section 3.1.1.

The salt detections toward G17 resemble that toward SrcI, with both NaCl and KCl tracing the same rotational structure. Figure 5 shows position-velocity diagrams perpendicular to the outflow axis measured by Maud et al. 2018 at position angle $\theta \approx 135°$ based on the large-scale CO outflow. Maud et al. (2019) measured the disk position angle to be 25.9°, which traces the direction of maximum gradient in the H_2O disk and through the emission peak of the continuum structure. This angle is nearly perpendicular to the large-scale outflow; we adopt this angle as the disk PA. Maud et al. (2019)

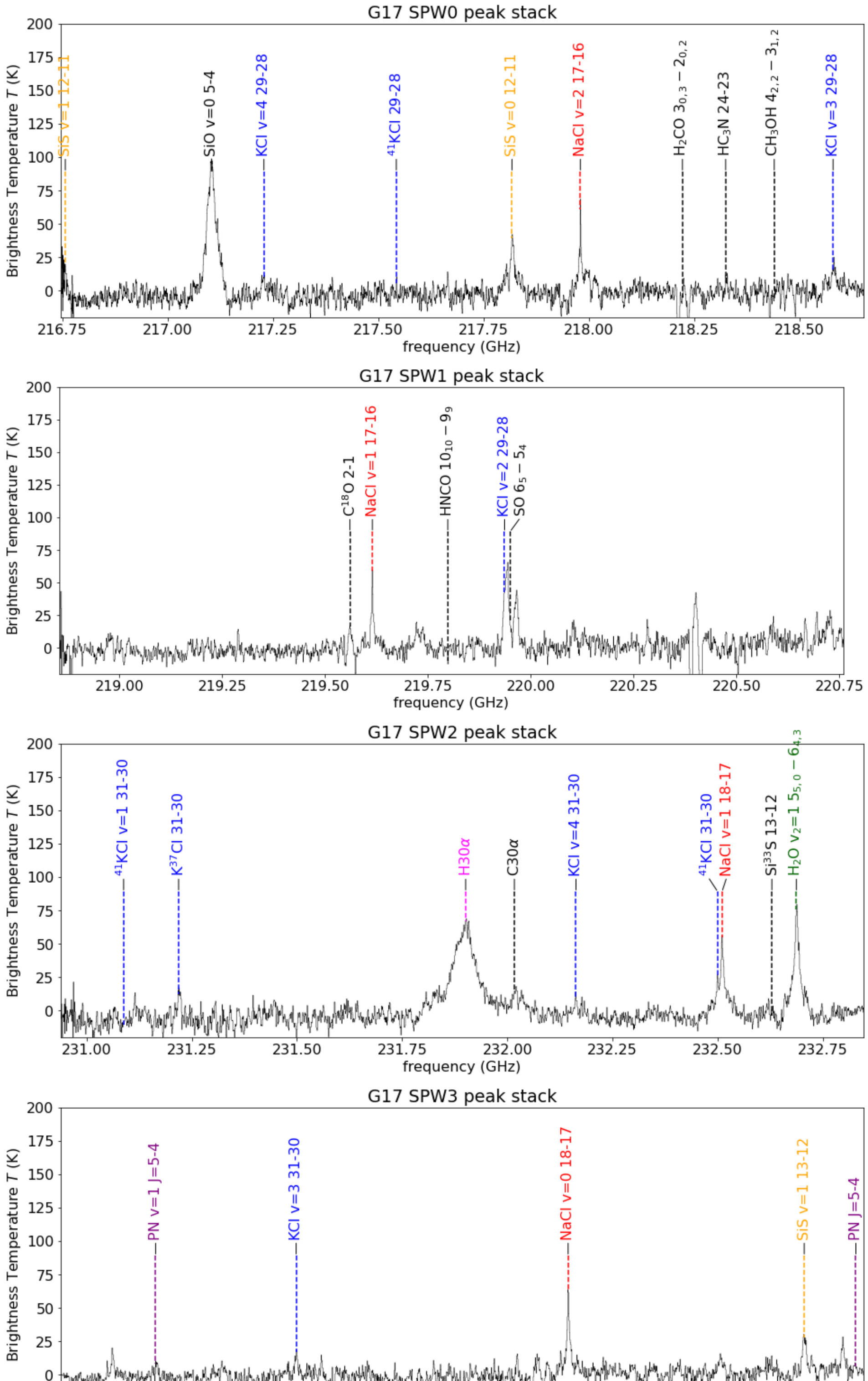

Figure 4. Stacked spectra toward G17 from the Maud et al. (2019) data set. The stacking was based on the H_2O line. Line IDs are shown. Different colors are used for targeted species with multiple transitions in-band: orange for SiS, blue for KCl, red for NaCl, magenta for H30α, purple for PN, and green for H_2O. The remaining species, with only one transition marked, are shown in black.

Table 2. Summary of spectroscopic lines used in this analysis

Line Name	Frequency GHz	E_U K
SiS v=1 12-11	216.757603	1138.75
SiO v=0 5-4	217.104980	31.26
KCl v=4 29-28	217.228912	1733.21
^{41}KCl 29-28	217.543178	156.71
SiS v=0 12-11	217.817644	67.95
NaCl v=2 17-16	217.979967	1128.38
$H_2CO\ 3_{0,3}-2_{0,2}$	218.222192	20.96
HC_3N 24-23	218.324788	1084.99
$CH_3OH\ 4_{2,2}-3_{1,2}$	218.440063	1422.49
KCl v=3 29-28	218.579708	1345.06
$C^{18}O$ 2-1	219.560354	15.81
NaCl v=1 17-16	219.614936	614.51
HNCO $10_{10}-9_9$	219.798274	58.02
KCl v=2 29-28	219.936113	671.38
SO 6_5-5_4	219.949440	34.98
$K^{37}Cl$ v=2 30-29	221.078543	948.25
^{41}KCl v=1 31-30	231.088150	572.25
$K^{37}Cl$ 31-30	231.218839	177.68
H30α	231.900928	-
C30α	232.016632	-
KCl v=4 31-30	232.163002	1755.14
^{41}KCl 31-30	232.499840	178.67
NaCl v=1 18-17	232.509950	625.67
$Si^{33}S$ 13-12	232.628545	78.16
H_2O v_2=1 $5_{5,0}-6_{4,3}$	232.686700	3461.91
$K^{37}Cl$ v=4 32-31	232.907553	1739.18
PN v=1 J=5-4	233.271800	1937.30
KCl v=3 31-30	233.605698	1367.12
NaCl v=0 18-17	234.251912	106.85
SiS v=1 13-12	234.812968	865.40
PN J=5-4	234.935663	33.83
KCl v=2 31-30	235.055578	687.16
$K^{37}Cl$ v=2 31-30	235.768235	970.53
SiS v=0 13-12	235.961363	79.28

Lines covered by one or more observations in this work. The frequency and upper state energy levels are pulled from Splatalogue and refer either to CDMS, SLAIM, or JPL values. For KCl v=3 and v=4 values, E_U is drawn from the modified version of the Barton et al. (2014) line list used in Ginsburg et al. (2019a).

measured the disk inclination to be $i = 40 \pm 4^\circ$ from the axis ratio of the continuum image, so we adopt that inclination when overplotting Keplerian curves. As with SrcI, both the water and salt lines trace out orbits consistent with Keplerian rotation around a high-mass star. Figure 6 shows integrated intensity (moment-0) and intensity-weighted velocity (moment-1) maps of the G17 disk.

G17 chemically resembles SrcI in several ways: the only lines seen directly toward the source are H_2O, NaCl, KCl, SiS, and SiO. There is little 'contamination' in the spectrum from COMs. As in SrcI, KCl lines are detected at about half the peak brightness of NaCl lines with similar E_U; no v=0, v=1, or v=2 transitions of KCl are covered by the observations (except KCl v=2 J=29-28, which is blended with SO 6_5-5_4 and cannot be clearly identified).

We measure enough lines to produce both rotational and vibrational diagrams for KCl, but only a rotational diagram for NaCl (Figure 7). These plots provide temperature and column density measurements of the target molecules if the observed transitions are in local thermodynamic equilibrium (LTE). As in SrcI, the rotational temperatures are much cooler ($T_{rot} \sim 35-60$ K) than the vibrational temperatures ($T_{vib} \sim 900$ K), indicating that non-LTE effects are important. We have yet to determine the underlying mechanism, but several possibilities are discussed in Ginsburg et al. (2019a). We defer further discussion of the excitation to a future work in which we will integrate additional transitions.

A key difference between SrcI and G17 is that G17 exhibits radio recombination line (RRL) emission, while SrcI does not. Figure 5 shows the H30α RRL in grayscale with NaCl contours on top, showing that the RRL comes from a smaller region contained within the NaCl-bearing disk.

Both SrcI and G17 have central 'holes' in which there is no NaCl emission. In SrcI, Ginsburg et al. (2019a) inferred the presence of this hole from the gas kinematics, as the *apparent* hole seen in Figure 1a is an observational effect caused by high optical depth in the edge-on dust disk. In G17, which is less inclined, the hole is directly observed (Figure 1b). Since the radiation field is more energetic in G17 than in SrcI, it is possible that the salt hole is related to the gas temperature.

3.3.2. *G351.77-0.54*

Beuther et al. (2017) and Beuther et al. (2019) published high-resolution observations of the G351.77-0.54 region, which we use here over the lower-resolution DIHCA data. We focus on the two brightest mm sources, mm1 and mm2, which both exhibit H_2O and salt line emission. G351mm2 is a substantially fainter source, but similarly exhibits brine lines. Spectra of the G351 sources and subsequent sources are presented in the Appendices.

We identify several lines in mm1, including NaCl v=1 and v=2 J=18-17 and SiS v=0 and v=1 J=13-12 (these

Table 3. Summary of detections, tentative detections, and non-detections of target species in the source sample

Source	disk	H_2O	NaCl	KCl	SiO	RRL	COMs	SiS	SO	PN
Orion SrcI	yes	yes	yes	yes	yes	no	no	yes	yes	?
G17	yes	yes	yes	yes	yes	yes	no	yes	yes*	no
I16547A	yes-c	yes	yes*	no	yes	no	yes	yes	yes	yes
I16547B	yes-c	yes	yes*	no	yes	no	yes	yes	yes	yes
G351.77mm1	yes-c	yes	yes	no	yes	no*	no	yes	no	yes
G351.77mm2	unres	yes	yes*	no	no	yes	no	no	no	no*
G351.77mm12	unres	yes	yes*	no	yes	no	no	yes	no	yes
W33A mm1-main	unres	yes*	yes*	no	yes	yes*	yes	yes*	yes	yes
NGC6334Imm1b	yes-c	yes	yes	yes	yes	no	yes*	yes	no*	yes*
G5.89 mm15	cont	no	no	no	?	no	no	no	no	no
IRAS18162 GGD27	yes	no	no	no	?	no	yes	no	yes	no
NGC6334IN SMA6	no	yes*	no	no	no	no	yes	no	no	yes*
NGC6334IN SMA1b/d	no	no*	no	no	no	no	yes	no	no	no*
G11.92mm1	yes	no	no	no	yes	no	yes	yes*	yes	yes*
IRAS18089 I18089-1732	yes-c	no	no	no	yes	no	yes	yes*	yes	no*
IRAS16562 G345.4938+01.4677	no	no	no	no	yes	yes	ext	no	ext	no
G333.23mm1	no	no	no	no	no*	no	yes	no	yes	yes*
G333.23mm2	yes*	no	no	no	no*	no	yes	no	yes	yes*
G335 ALMA1	no	no	no	no	yes	no	yes	no	no*	no
G29.96 submm1	no	no	no	no	yes	no	yes	no*	no*	no*
G34.43mm1	no	no	no	no	no*	no*	yes	no	yes	no*
S255IR SMA1	no*	no*	no	no	yes	yes	yes	no	yes	no
NGC6334Imm1d	yes*	yes*	no	no	no	no	no	no	no	yes*
NGC6334Imm2b	unres	yes	no*	no	yes	no	yes	yes	yes	yes*

We use '?' to indicate "not observed", 'yes' for a definitive detection, 'no' for definitive non-detections, 'yes*' for tentative detections, and 'no*' for tentative nondetections, where this uncertainty can either be from line confusion or low signal-to-noise, and 'ext' for those associated with the envelope but not the disk. These all refer to detections in emission; COMs are seen in absorption toward many sources, but we do not consider these. For SiO, we do not attempt to distinguish between SiO from the outflow and from the disk; in Orion SrcI, we know that SiO is present in both. For the 'disk' column, we either answer 'yes' for a clear disk detection from literature kinematic characterization, 'yes-c' for a candidate disk toward which a kinematic signature consistent with rotation has been observed, but for which the kinematics have not yet been confirmed to be Keplerian, 'continuum' if a disk-like (linear, $\lesssim 300$ au long) feature is seen in the continuum, 'unresolved' if the targeted source is too small for us to say, and 'no' if neither of the above hold; 'no' does not indicate that no disk is present, merely that we did not identify one. In many cases, we suspect a disk must be present because there is an outflow, but we say 'no' if we can't see it.

latter were clearly detected, and used for disk kinematic study, in Beuther et al. (2019), but were listed as 'unidentified'). Because of the slightly different spectral configuration adopted in these observations as compared to the DIHCA observations, both the J=12-11 and J=13-12 lines of SiS v=0 are covered and detected.

The morphology and range covered by NaCl and SiS are very similar (Appendix A.1), though the gap in the center for SiS is more pronounced than for NaCl. These molecules arise in similar, but not identical, regions.

The velocity gradients in NaCl, H_2O, and SiS in mm1 appear to trace a bipolar outflow. Beuther et al. (2019) discussed the SiS emission lines in detail, comparing the velocity gradient observed in this line to that seen in SiO. The SiO J=5-4 and CO J=6-5 lines both appear in an extended redshifted lobe to the northwest of the source. The outflow is asymmetric and truncates at the position of mm1, suggesting that mm1 is the source (Beuther et al. 2017). Since the redshifted lobe occurs on the redshifted side of the observed SiS velocity gradient, Beuther et al. (2019) interpreted the lines as part of an outflow rather than a disk. While there is a blueshifted component opposite the redshifted flow, it is detected in only two channels and is only seen in the beam adjacent to the central source, so its direction cannot be determined independent from the elongated red lobe. They also noted the presence of a velocity gradient perpendicular to the outflow direction in CH_3CN, suggesting that CH_3CN traces the disk in a disk-outflow system. The observed velocity gradient in briny lines is perpendicular

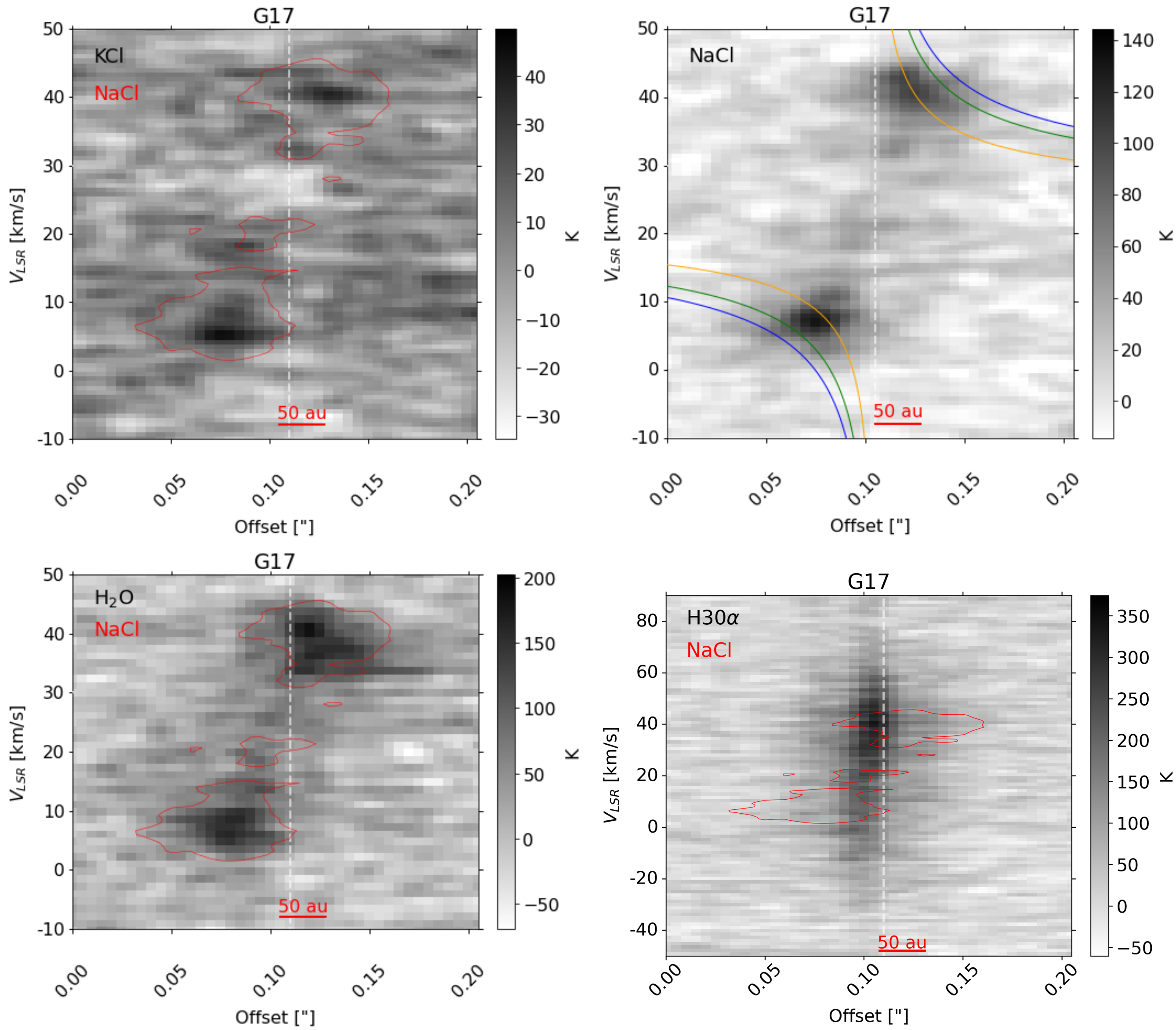

Figure 5. Position-velocity diagrams extracted across the G17 disk. (top left) KCl grayscale with NaCl contours (top right) NaCl grayscale with Keplerian rotation curves drawn for a 15, 30, 40 $M_\odot$ star with a $i = 40°$ disk (Maud et al. 2019) in orange, green, and blue, respectively. (bottom left) Water (H_2O) in grayscale with thin NaCl contours. In all cases, the velocity gradient matches that of the disk identified in Maud et al. (2019). (bottom right) Position-velocity diagram of the H30α line toward G17, with NaCl contours overlaid. The H30α emission is clearly confined to within the NaCl disk. While there is a hint of a velocity gradient in the H30α line, it is unclear whether this gradient traces rotation.

to the CH_3CN disk, indicating either that the emission comes from outflow or that the disk changes orientation with scale.

We re-examine the kinematics of the now-identified lines here. Figure 8 shows moment-0 and moment-1 maps of both NaCl (stacked) and H_2O. The kinematics resemble a disk, with kinematics consistent with orbital motion around a $\sim 20/\sin i\ M_\odot$ central potential, However, the extended SiO / CO J=6-5 outflow feature is parallel, rather than perpendicular, to the axis of the velocity gradient. Assuming the SiO structure is tracing an outflow, the velocity structure seen in Figure 8 is the base of the outflow. The lack of any gradient perpendicular to the outflow direction suggests that the briny lines are not tracing a disk wind in G351mm1, as they are in SrcI (Hirota et al. 2017), since they would retain that rotation signature for at least some distance above the disk. However, the lines are marginally resolved and extended in the direction perpendicular to the outflow, suggesting that the emission arises from an area at least

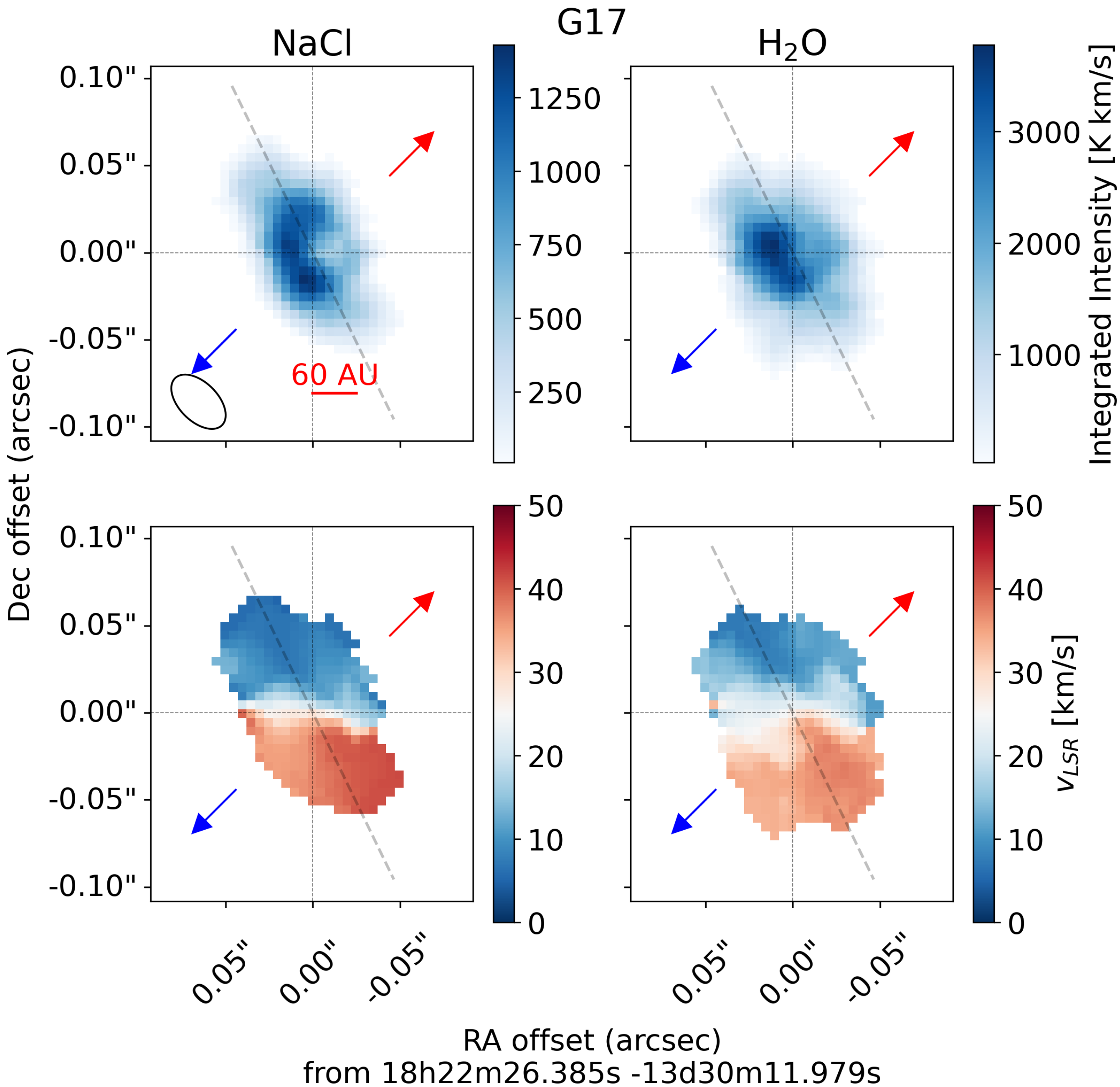

Figure 6. Moment-0 (integrated intensity) and moment-1 (intensity-weighted velocity) images of stacked NaCl (left) and H_2O (right) for G17. The red and blue arrows indicate the outflow direction from Maud et al. (2017). The dashed gray line shows the direction the position-velocity diagram was extracted from (Figure 5).

comparable to be beam size ($\sim$ 50 AU). The extended launching region is difficult to reconcile with the lack of disklike kinematics. We are not able to definitively conclude on the nature of the velocity gradient in mm1 and suggest that it should be studied further at high resolution, particularly to trace the kinematics of the disk-outflow system(s). Nevertheless, we note that the briny emission is limited to a region $<$ 100 AU across.

By contrast to mm1, mm2 has H_2O emission (Appendix A.2), but only tentative NaCl emission (the v=1 line is detected at $\sim$ few $-\ \sigma$, but the v=2 line is below the noise). No SiS emission is detected. However, H30α emission is fairly clearly detected. There is a velocity gradient along the NW-SE axis in the H_2O line (Appendix A.2). Curiously, this is perpendicular to the direction of the gradient shown in Figure 9 of Beuther et al. (2019), which shows the unidentified 231.986 GHz

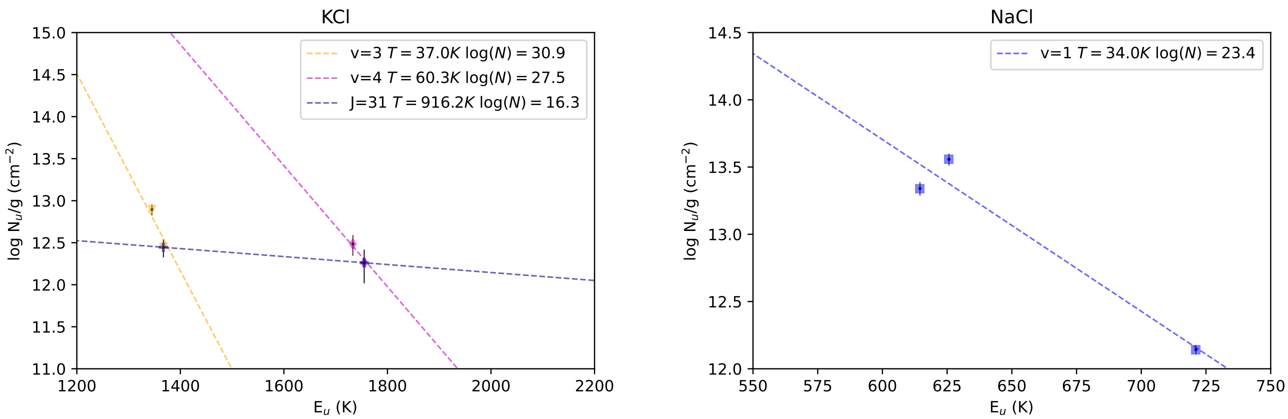

Figure 7. Rotation diagrams from the fitted lines toward G17. (left) KCl rotation diagram (right) NaCl rotation diagram

line, suggesting that there may be perpendicular gradients here tracing outflow and disk. However, no outflow is known toward this source, and we do not see clear signs of outflow in any of the lines studied here, including SiO. While SiO is detected in emission and absorption toward mm1, it is detected only in absorption toward mm2.

Despite the presence of many KCl transitions in band, there are no detections - but our limits on these lines are relatively weak, as all of the v=0 and v=1 transitions tend to land in confused regions or come from doubly-rare isotopologues.

A third source, G351mm12, also has salt detected. Appendix A.3 shows the standard suite of figures for this detection. This source is barely resolved. Its moment maps indicate a hint of velocity gradient, but the gradient is at the limit of our sensitivity and may be spurious.

3.3.3. *NGC6334I*

There are three sources within the NGC 6334I region that may exhibit brine emission. Sources mm1b and mm2b are both notable for being faint continuum sources adjacent to bright sources identified in lower-resolution data (the 'b' designation indicates that there are sources mm1a and mm2a that are brighter).

mm1b exhibits clear signatures of H_2O, multiple NaCl lines, SiS, and several likely KCl detections (Appendix A.4). The H_2O line shows hints of rotation perpendicular to the outflow axis (Fig. 8 of Brogan et al. (2018) shows the outflow, which is aligned to PA $\approx 0°$ to $-5°$, close to straight north-south), though the other lines do not as clearly exhibit this signature. Brogan et al. (2018) note several other less prominent outflows centered on this source, however, which hints that this object cannot be interpreted as a single disk-outflow system. In the PV diagram of NaCl (Fig. 9), we show curves at 10, 20, and 30 $M_\odot$ for an edge-on Keplerian disk. Since the emission is confined to lower velocities than the 10 $M_\odot$ curve, it appears that this source is $< 10\ M_\odot$. However, it may also be significantly inclined to the line of sight, in which case it may be more massive. KCl is tentatively detected toward mm1b, with reasonably strong peaks appearing in the KCl v=2 J=29-28 and $K^{37}Cl$ v=0 J=31-30 lines. Some others that might be expected to be bright, e.g., KCl v=3 J=29-28 and v=3 J=31-30, are ambiguous or blended.

The other sources are less clear detections and are therefore considered only candidate brinary sources. Similar to mm1b, mm2b has a reasonably clear H_2O detection and strong signs of SiS v=0 J=12-11 emission, but it has no clear detection of any salt line (Appendix A.4). No clear outflow is present. The SiS line profile is broad and somewhat different from that of water, so it is not obvious that they trace the same kinematics.

mm1d has only has marginal SiS and H_2O detections. We do not include it in the figures or detection statistics. It is a strong candidate for follow-up observations.

3.3.4. *W33A*

We marginally detect H_2O, H30α, and NaCl toward the bright source at the center of W33A (Appendix A.5). At the current resolution, the emitting region is unresolved. The detection of any of these lines individually is tentative because we have only one firm line detection for each of these molecules and they are potentially blended with other emission lines. The PN 5-4, H_2O, and NaCl v=1 18-17 lines are the most prominently detected. The NaCl v=1 and v=2 J=17-16 lines are too weak to confirm the NaCl detection. While we detect only one PN line, it is isolated enough that confusion is unlikely to affect it, so it is a reasonably firm detection. This source is a prime candidate for further followup.

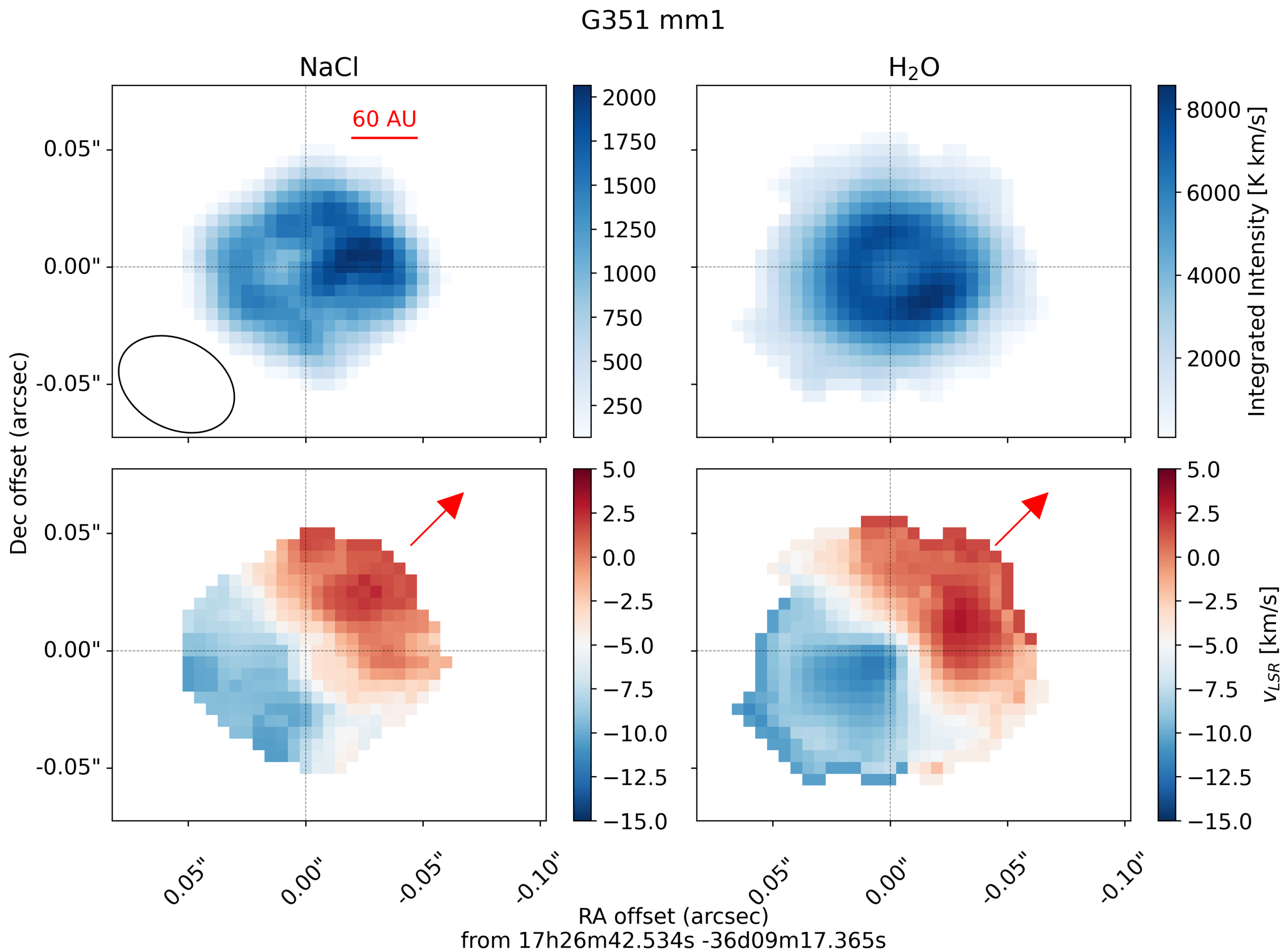

Figure 8. Moment-0 (integrated intensity) and moment-1 (intensity-weighted velocity) images of stacked NaCl (left) and H_2O (right) for G351 mm1. The position-velocity diagrams in Figure 14 are taken along position angle 130°, parallel to the velocity gradient seen in the lower panels here. The red arrow shows the direction of the outflow from Beuther et al. (2019) that extends $\gtrsim 0.2$ pc to the northwest. A compact blueshifted feature was also weakly detected bin SiO opposite the redshifted flow, but it is unresolved. The blue side of the NaCl, H_2O, and (in Appendix A.1) SiS and PN corresponds with the SiO blueshifted lobe seen in Fig. 7 of Beuther et al. (2019), but since its extent is limited to the $\lesssim 100$ AU scale shown in this figure, we cannot confirm whether it is comprised of outflowing material.

3.3.5. *I16547*

I16547A and B were reported to have salt, water, and SiS emission in Tanaka et al. (2020). We confirm their detections both with their original data and with coarser-resolution observations from the DIHCA program. Despite the clear detection of those three briny species (see spectra in Appendix A.6 and A.7), there is no sign of KCl in the data. The non-detection is in part driven by confusion, in that many of the lower-J transitions of KCl lay atop transitions from other molecular species that are spatially extended and not filtered out. Line stacking was not very helpful for these two targets because they are only marginally resolved (Fig. 2). Nevertheless, velocity gradients consistent with rotation are apparent in position-velocity diagrams extracted along the direction of the maximum gradient (Appendices A.6 and A.7), which is perpendicular to the outflow direction (Tanaka et al. 2020), suggesting that these are both likely disks around high-mass YSOs.

3.4. *Unsalted sources*

The remainder of our targets do not have salt or water detections. We describe them in slightly more detail in Appendix B. We note here that several of these, i.e., G11.92, GGD27, and I18089, have clear extended disks that are detected in other molecules (e.g., CH_3CN) but not in brinary lines.

4. DISCUSSION

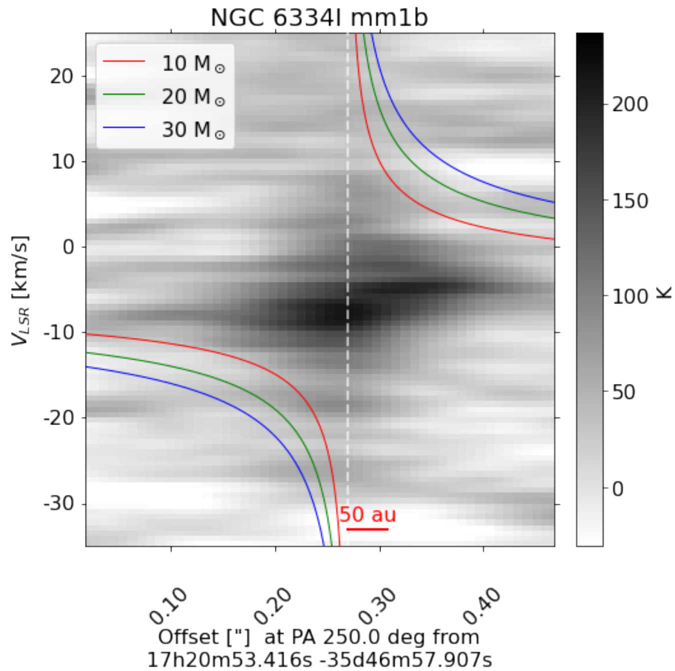

Figure 9. Position-velocity diagram of NaCl in the NGC 6334I mm1b disk. Keplerian velocity curves for edge-on 10, 20, and 30 $M_\odot$ central potentials are overplotted; the central potential here appears to have $M \sin i < 10\ M_\odot$.

4.1. *Are briny lines disk-only tracers?*

Many of our targets are only candidate disk sources, in that no resolved Keplerian rotation curve has been observed. We therefore consider the question: Could the briny emission be from outflows? Under the assumption that outflows are driven by either a wind from a disk or from accretion from a disk onto a star, the presence of an outflow still indicates the presence of a disk, but that does not mean the lines we observe necessarily arise within that disk.

In SrcI, it is clear that the water is partly outflowing, but it arose from a disk wind and had a small observable scale height ($h < 40$ au; see Fig. 10 of Ginsburg et al. 2018). Even in that case, the water line was dominated by disk kinematics, not outflow.

In most of the observed sources, a velocity gradient across the lines of interest was observed. Such a velocity gradient can be produced by either outflow ejection or disk rotation. In the best-resolved cases, G17 and G351, the emission forms a complete ring, which is expected of a disk or disk wind. The circular extent of the briny emission shows that it is not tracing a collimated jet feature. However, in G351mm1, the direction of the gradient is along the known outflow, suggesting that the briny lines do not trace a disk or a disk wind; this source remains difficult to interpret.

While we cannot definitively determine the general origin of briny emission, we observe here that it is restricted to radii < 300 au in our full sample, such that it is always consistent with arising in either the disk or the very inner portion of the outflow.

4.2. *Chemical similarities between the salt disks*

We examine the general chemical properties of the brinary disks. Each has several properties in common, but several differences. Table 3 lists the detections and non-detections toward each examined source. We observe that NaCl, H_2O, and SiS lines are often detected toward the same sources, and generally if one is absent, all are. In other words, they exhibit comparable brightness when they are observed. This correlation hints that they come from similar regions within disks or outflows, either because of excitation or chemical (formation/destruction) conditions.

Figure 10 shows the cross-correlation of the boolean value ("yes" or "no") encoded in table 3; the tentative detections marked with '*'s are assigned to their corresponding 'yes' or 'no' prefix. It shows that the presence of NaCl, SiS, and H_2O are strongly correlated. The presence of COMs in the spectra is moderately anti-correlated with these 'brinary' species. RRLs are strongly anti-correlated with COMs. The correlations among the other molecules (and RRLs) are less pronounced.

We note that our data are extremely incomplete, as we explicitly select against COM-bearing targets by selecting H_2O-bearing disks. There are many fainter disk

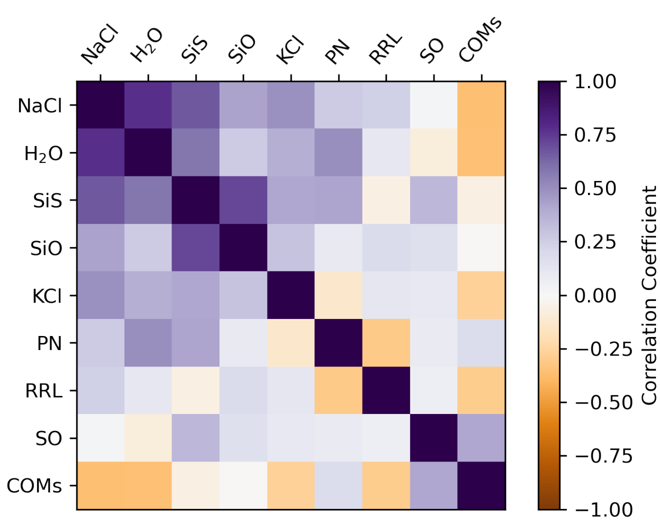

Figure 10. Cross-correlation plot made from Table 3. We cross-correlate purely on the boolean value; those with a 'yes' are marked True, and those without a 'yes' are marked False. The rows are sorted in order of correlation with NaCl.

candidates in the fields of view of our observations that we did not include in our sample or in this plot. Most of these sources do exhibit COM emission and do not exhibit RRL emission, though, so adding them to this plot would generally strengthen the trends shown.

Because of the incompleteness of our sample, we caution against over-interpretation. A repeat of this analysis with a consistently-selected sample will be needed to draw firm conclusions. However, the correlations in the top-left of the plot, between H_2O, NaCl, and SiS appear firm - these species coexist in this sample of disk candidates.

4.2.1. *The low detection rate of KCl is an observational effect*

The KCl detections are not perfectly correlated with NaCl detections, but we argue here that this is an observational selection effect. Most likely, KCl is better-correlated with NaCl than is apparent in Figure 10.

In the targeted band, there are no v=1 or v=0 transitions of the most common isotopologue (^{39}K-^{35}Cl) of KCl, such that all detections are of higher-excitation, lower-brightness transitions. The targeted KCl lines are also partly hidden by confusion with other lines. The KCl lines are strongly anti-correlated with the presence of COMs, which is primarily (or entirely) because of confusion: the KCl lines in this band are weaker than NaCl when they are detected, so they are more difficult to distinguish from the molecular line forest present in dense spectra. They land inconveniently near bright COM lines in the 215-235 GHz range more often than the NaCl lines.

The comparison to SrcI illustrates some of these effects. In SrcI, the peak brightness temperature of the NaCl and KCl lines with $E_U < 1000$ K were similar, with $T_{\rm B,max} \sim 100 - 200$ K. The NaCl v=0 lines were no more than twice as bright as the KCl v=0 lines. The SrcI data set was targeted on outflow-tracing lines, including ^{12}CO J=2-1 and SiO v=1 J=5-4, which both have nearby v=0 and v=1 KCl transitions, while the DIHCA observations and others presented here chose to target the CH_3CN ladder at 220.4 GHz and therefore did not cover these low-v transitions.

4.2.2. *PN in the brine*

The PN J=5-4 line appears to be detected in several of our sources. The PN v=1 J=5-4 transition, at 233.27182 GHz, is not detected. For the line-poor brinaries, there is little confusion around this line, and its velocity lines up perfectly with that of salts, so this identification is reasonably certain. For the rest of the sample, the case is less clear; while there are some tentative detections with clear lines at this velocity, the spectra are so rich that we cannot definitively identify PN as the carrier species. The presence of PN in the same regions as the highly-excited salt lines may suggest that PN occupies a similar location within and binding energy to dust grains. Rivilla et al. (2020) suggest that PN is present in the cavity walls of an outflow toward AFGL 5142, but that it is released to the gas phase as PH_3, and the PN molecules are subsequently formed under the influence of the star's UV radiation. Given the lack of UV photons in these sources, as indicated by the lack of correlation between PN and RRLs in Figure 10, our data may indicate that PN is present in the grains and not formed in the gas phase.

4.2.3. *RRLs*

Hydrogen recombination lines are likely to be produced in the ionized regions surrounding accreting high-mass young stars once they have contracted onto the main sequence. In our sample, few RRLs are detected. Their presence, or absence, is only weakly anti-correlated with the presence of COMs and PN, but has little correlation with other molecules. While we might expect RRL emission to become detectable from accreting HMYSOs toward the end of their accretion phase, as the ionization rate is able to overtake the accretion rate of fresh neutral material, our data provide little evidence for this process.

4.3. *Excitation*

At least in the best-resolved cases, G17 and G351, vibrationally excited states of NaCl are detected (v=1, and 2). This feature is in common with SrcI, where states up to v=6 were convincingly detected. The v=2 detections in particular, with $E_{\rm U} \gtrsim 1000$ K, suggest that an excitation pattern similar to that in SrcI, in which $T_{\rm vib} > T_{\rm rot}$, is common. This general feature is also common in evolved stars that exhibit salt emission, suggesting that these salt lines only appear in regions with strong radiative backgrounds in the infrared. Figure 7 highlights the high excitation, though we defer deeper analysis of the excitation properties to a future work.

4.4. *Spatial Resolution*

Our observed sample has non-uniform spatial resolution (Table 1), which helps explain several of the non-detections. We show a version of Figure 1 with all images resized to the same physical scale shown in Figure 11, highlighting that the detected NaCl disks are small. We did not detect NaCl toward any sources observed with beam size $>$ 300 au, which included four of our targeted fields. Five of the fifteen targeted fields included detections. We performed a logistic regression of

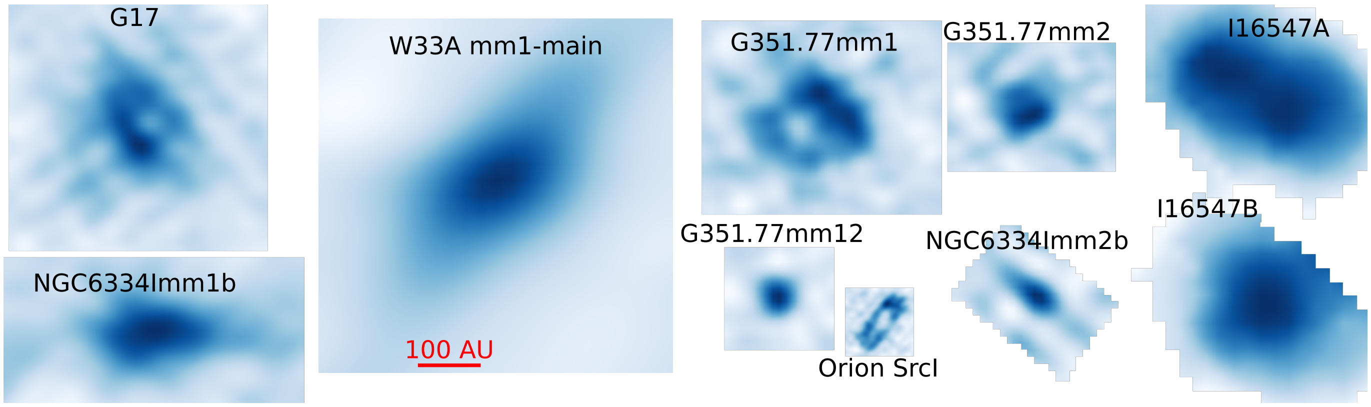

Figure 11. The integrated intensity (moment-0) maps of NaCl shown in Fig. 1 and 2, but now with each image scaled to the same physical resolution. The 100 AU scalebar, shown on the W33A mm1-main panel, applies to all panels. The intensity scales are arbitrary, as the intent is only to show the disk candidate structure.

the detection of salt against resolution and found that the likelihood of salt detection in our sample is $> 50\%$ for resolution < 120 au, peaking at $\sim 80\%$ at infinite resolution. While our haphazard sample selection prevents drawing strong conclusions, these results suggest that salty regions are limited to small scales ($\lesssim 300$ au) and are challenging to observe if they are not well-resolved. This observational limitation highlights the need for more extensive extremely high-resolution observations with ALMA's longest-baseline configurations to obtain dynamical mass measurements for high-mass YSOs.

It is possible that more sensitive observations with poor physical resolution may detect brinary lines now that we know to look for them. However, the main difficulty in detecting these lines is not raw sensitivity, but confusion with other lines. It will be beneficial to search other parts of the spectrum for more isolated brinary lines, which might be expected to be more common at lower frequencies. It may be possible to determine the presence or absence of brinary lines by stacking the various transitions across species to average down the 'contaminant' noise provided by other lines; we leave investigation of this possibility to future work.

5. CONCLUSIONS

- We have substantially increased the number of high-mass protostellar objects with detection of salt, hot water, and SiS, increasing the number from three to nine published detections across six regions.

- Salt, water, and SiS tend to coexist. PN may also coexist with these species. When any of these molecules is detected in a HMYSO disk, all of them are likely to be.

- Brinary sources are line-poor compared to typical hot cores. The lack of COMs in the briny regions suggests that the chemistry of these regions is different from hot cores, even when the central objects are surrounded by hot cores.

- These emission lines do not come from the same volume as ionized hydrogen. While some of the HMYSO candidates targeted exhibit both RRL and brine emission, the presence of an RRL is a poor predictor of whether NaCl and H_2O are detected. The resolved case of G17 shows that the ionized gas comes from a smaller radius than the NaCl.

- With the nine brinaries presented here, we demonstrate that salt emission is not rare. The primary reason it is not often detected is resolution: the emission comes exclusively from small ($\lesssim 100$ au) size scales, confirming that either chemistry or excitation restricts the millimeter lines described here to disk-sized regions. Line confusion limits our ability to detect these lines even when they are present, though confusion can be alleviated with high spatial resolution.

- However, salt and water emission is also not ubiquitous in HMYSO disks. Some of the most compelling Keplerian disks around HMYSOs in the literature, such as GGD27 and G11.92mm1, show no sign of salt emission despite their similarities to other disks and superior data quality.

There is clearly substantial future work to do with these data and expanded samples of brinaries. Some of the more obvious questions about brinary lines include:

- Are they correlated with source luminosity or stellar mass?

- What disks, or outflows, produce them?
- Do they occur around low-mass YSOs?
- Why are highly vibrationally excited lines ($v > 3$) detected?

Many of these questions will require establishing less biased, more systematic samples of YSO candidates. Others will require more detailed, multi-line studies toward a limited sample.

Acknowledgements We thank the anonymous referee for a thorough and constructive report that significantly improved the paper, particularly in terms of structure and readability. AG acknowledges support from NSF AAG 2008101 and NSF CAREER 2142300. HB acknowledges support from the European Research Council under the European Community's Horizon 2020 frame-work program (2014-2020) via the ERC Consolidator Grant 'From Cloud to Star Formation (CSF)' (project number 648505). HB also acknowledges support from the Deutsche Forschungsgemeinschaft (DFG, German Research Foundation) – Project-ID 138713538 – SFB 881 ("The Milky Way System", subproject B01). P.S. was partially supported by JSPS KAKENHI grant Nos. JP18H01259 and JP22H01271. K.E.I.T. acknowledges support by JSPS KAKENHI grant Nos. JP19K14760, JP19H05080, JP21H00058, and JP21H01145.

This paper makes use of the following ALMA data: ADS/JAO.ALMA#2016.1.01036.S, ADS/JAO.ALMA#2017.1.00237.S, ADS/JAO.ALMA#2016.1.00550.S, ADS/JAO.ALMA#2019.1.00492.S, ADS/JAO.ALMA#2017.1.00098.S, ADS/JAO.ALMA#2018.1.01656.S, and ADS/JAO.ALMA#2013.1.00260.S. ALMA is a partnership of ESO (representing its member states), NSF (USA) and NINS (Japan), together with NRC (Canada), MOST and ASIAA (Taiwan), and KASI (Republic of Korea), in cooperation with the Republic of Chile. The Joint ALMA Observatory is operated by ESO, AUI/NRAO and NAOJ. In addition, publications from NA authors must include the standard NRAO acknowledgement: The National Radio Astronomy Observatory is a facility of the National Science Foundation operated under cooperative agreement by Associated Universities, Inc.

Software: The source code underlying this work are available from github This work used CARTA (Comrie et al. 2021), Jupyter notebooks (Kluyver et al. 2016). numpy (van der Walt et al. 2011; Harris et al. 2020), scipy (Virtanen et al. 2020), astropy (Astropy Collaboration et al. 2013, 2018; The Astropy Collaboration et al. 2022), spectral-cube (Ginsburg et al. 2019b), radio-beam (Koch et al. 2021), and CASA-6 (https://casa.nrao.edu/casadocs/casa-5.6.0/introduction/casa6-installation-and-usage). matplotlib (Hunter 2007), astroquery (Ginsburg et al. 2019c), and pyspeckit (Ginsburg et al. 2022).

REFERENCES

Añez-López, N., Osorio, M., Busquet, G., et al. 2020, ApJ, 888, 41, doi: 10.3847/1538-4357/ab5dbc

Astropy Collaboration, Robitaille, T. P., Tollerud, E. J., et al. 2013, A&A, 558, A33, doi: 10.1051/0004-6361/201322068

Astropy Collaboration, Price-Whelan, A. M., Sipőcz, B. M., et al. 2018, AJ, 156, 123, doi: 10.3847/1538-3881/aabc4f

Barton, E. J., Chiu, C., Golpayegani, S., et al. 2014, MNRAS, 442, 1821, doi: 10.1093/mnras/stu944

Beltrán, M. T., Cesaroni, R., Neri, R., & Codella, C. 2011, A&A, 525, A151, doi: 10.1051/0004-6361/201015049

Beltrán, M. T., & de Wit, W. J. 2016, A&A Rv, 24, 6, doi: 10.1007/s00159-015-0089-z

Beuther, H., Walsh, A. J., Johnston, K. G., et al. 2017, A&A, 603, A10, doi: 10.1051/0004-6361/201630126

Beuther, H., Zhang, Q., Bergin, E. A., et al. 2007, A&A, 468, 1045, doi: 10.1051/0004-6361:20066954

Beuther, H., Zhang, Q., Sridharan, T. K., & Chen, Y. 2005, ApJ, 628, 800, doi: 10.1086/431277

Beuther, H., Hunter, T. R., Zhang, Q., et al. 2004, ApJL, 616, L23, doi: 10.1086/383570

Beuther, H., Ahmadi, A., Mottram, J. C., et al. 2019, A&A, 621, A122, doi: 10.1051/0004-6361/201834064

Brogan, C. L., Hunter, T. R., Cyganowski, C. J., et al. 2018, ApJ, 866, 87, doi: 10.3847/1538-4357/aae151

Cernicharo, J., & Guelin, M. 1987, A&A, 183, L10

Chibueze, J. O., Omodaka, T., Handa, T., et al. 2014, ApJ, 784, 114, doi: 10.1088/0004-637X/784/2/114

Comrie, A., Wang, K.-S., Hsu, S.-C., et al. 2021, CARTA: The Cube Analysis and Rendering Tool for Astronomy, 2.0.0, Zenodo, Zenodo, doi: 10.5281/zenodo.3377984

Danilovich, T., Van de Sande, M., Plane, J. M. C., et al. 2021, A&A, 655, A80, doi: 10.1051/0004-6361/202141757

Decin, L., Richards, A. M. S., Millar, T. J., et al. 2016, A&A, 592, A76, doi: 10.1051/0004-6361/201527934

Fernández-López, M., Sanhueza, P., Zapata, L. A., et al. 2021, ApJ, 913, 29, doi: 10.3847/1538-4357/abf2b6

Ginsburg, A., Bally, J., Goddi, C., Plambeck, R., & Wright, M. 2018, ApJ, 860, 119, doi: 10.3847/1538-4357/aac205

Ginsburg, A., McGuire, B., Plambeck, R., et al. 2019a, ApJ, 872, 54, doi: 10.3847/1538-4357/aafb71

Ginsburg, A., Sokolov, V., de Val-Borro, M., et al. 2022, AJ, 163, 291, doi: 10.3847/1538-3881/ac695a

Ginsburg, A., Koch, E., Robitaille, T., et al. 2019b, radio-astro-tools/spectral-cube: Release v0.4.5, v0.4.5, Zenodo, Zenodo, doi: 10.5281/zenodo.3558614

Ginsburg, A., Sipőcz, B. M., Brasseur, C. E., et al. 2019c, AJ, 157, 98, doi: 10.3847/1538-3881/aafc33

Girart, J. M., Estalella, R., Fernández-López, M., et al. 2017, ApJ, 847, 58, doi: 10.3847/1538-4357/aa81c9

Girart, J. M., Fernández-López, M., Li, Z. Y., et al. 2018, ApJL, 856, L27, doi: 10.3847/2041-8213/aab76b

Guzmán, A. E., Sanhueza, P., Zapata, L., Garay, G., & Rodríguez, L. F. 2020, ApJ, 904, 77, doi: 10.3847/1538-4357/abbe09

Harris, C. R., Millman, K. J., van der Walt, S. J., et al. 2020, Nature, 585, 357, doi: 10.1038/s41586-020-2649-2

Highberger, J. L., Thomson, K. J., Young, P. A., Arnett, D., & Ziurys, L. M. 2003, ApJ, 593, 393, doi: 10.1086/376446

Hirota, T., Machida, M. N., Matsushita, Y., et al. 2017, Nature Astronomy, 1, 0146, doi: 10.1038/s41550-017-0146

Homan, W., Montargès, M., Pimpanuwat, B., et al. 2020, A&A, 644, A61, doi: 10.1051/0004-6361/202039185

Hunter, J. D. 2007, Computing in Science and Engineering, 9, 90, doi: 10.1109/MCSE.2007.55

Ilee, J. D., Cyganowski, C. J., Brogan, C. L., et al. 2018, ApJL, 869, L24, doi: 10.3847/2041-8213/aaeffc

Kalcheva, I. E., Hoare, M. G., Urquhart, J. S., et al. 2018, A&A, 615, A103, doi: 10.1051/0004-6361/201832734

Kauffmann, J., & Pillai, T. 2010, ApJL, 723, L7, doi: 10.1088/2041-8205/723/1/L7

Kluyver, T., Ragan-Kelley, B., Pérez, F., et al. 2016, in IOS Press, 87–90, doi: 10.3233/978-1-61499-649-1-87

Koch, E., Ginsburg, A., AKL, et al. 2021, radio-astro-tools/radio-beam: v0.3.3, v0.3.3, Zenodo, Zenodo, doi: 10.5281/zenodo.4623788

Kurayama, T., Nakagawa, A., Sawada-Satoh, S., et al. 2011, PASJ, 63, 513, doi: 10.1093/pasj/63.3.513

Liu, H.-L., Sanhueza, P., Liu, T., et al. 2020a, ApJ, 901, 31, doi: 10.3847/1538-4357/abadfe

Liu, S.-Y., Su, Y.-N., Zinchenko, I., et al. 2020b, ApJ, 904, 181, doi: 10.3847/1538-4357/abc0ec

Maud, L. T., Hoare, M. G., Galván-Madrid, R., et al. 2017, MNRAS, 467, L120, doi: 10.1093/mnrasl/slx010

Maud, L. T., Cesaroni, R., Kumar, M. S. N., et al. 2018, A&A, 620, A31, doi: 10.1051/0004-6361/201833908

—. 2019, A&A, 627, L6, doi: 10.1051/0004-6361/201935633

McMullin, J. P., Waters, B., Schiebel, D., Young, W., & Golap, K. 2007, in Astronomical Society of the Pacific Conference Series, Vol. 376, Astronomical Data Analysis Software and Systems XVI, ed. R. A. Shaw, F. Hill, & D. J. Bell, 127

Milam, S. N., Apponi, A. J., Woolf, N. J., & Ziurys, L. M. 2007, ApJL, 668, L131, doi: 10.1086/522928

Olguin, F. A., Sanhueza, P., Ginsburg, A., et al. 2022, ApJ, 929, 68, doi: 10.3847/1538-4357/ac5bd8

Olguin, F. A., Sanhueza, P., Guzmán, A. E., et al. 2021, ApJ, 909, 199, doi: 10.3847/1538-4357/abde3f

Peretto, N., Fuller, G. A., Duarte-Cabral, A., et al. 2013, A&A, 555, A112, doi: 10.1051/0004-6361/201321318

Qiu, K., Wyrowski, F., Menten, K., Zhang, Q., & Güsten, R. 2019, ApJ, 871, 141, doi: 10.3847/1538-4357/aaf728

Reid, M. J., Menten, K. M., Brunthaler, A., et al. 2014, ApJ, 783, 130, doi: 10.1088/0004-637X/783/2/130

Rivilla, V. M., Drozdovskaya, M. N., Altwegg, K., et al. 2020, MNRAS, 492, 1180, doi: 10.1093/mnras/stz3336

Rodríguez-Kamenetzky, A., Carrasco-González, C., Araudo, A., et al. 2017, ApJ, 851, 16, doi: 10.3847/1538-4357/aa9895

Sadaghiani, M., Sánchez-Monge, Á., Schilke, P., et al. 2020, A&A, 635, A2, doi: 10.1051/0004-6361/201935699

Sánchez Contreras, C., Alcolea, J., Rodríguez Cardoso, R., et al. 2022, arXiv e-prints, arXiv:2206.12185. https://arxiv.org/abs/2206.12185

Sánchez-Monge, Á., Schilke, P., Ginsburg, A., Cesaroni, R., & Schmiedeke, A. 2018, A&A, 609, A101, doi: 10.1051/0004-6361/201730425

Sanhueza, P., Garay, G., Bronfman, L., et al. 2010, ApJ, 715, 18, doi: 10.1088/0004-637X/715/1/18

Sanhueza, P., Jackson, J. M., Foster, J. B., et al. 2012, ApJ, 756, 60, doi: 10.1088/0004-637X/756/1/60

Sanhueza, P., Girart, J. M., Padovani, M., et al. 2021, ApJL, 915, L10, doi: 10.3847/2041-8213/ac081c

Sato, M., Wu, Y. W., Immer, K., et al. 2014, ApJ, 793, 72, doi: 10.1088/0004-637X/793/2/72

Stephens, I. W., Jackson, J. M., Sanhueza, P., et al. 2015, ApJ, 802, 6, doi: 10.1088/0004-637X/802/1/6

Tachibana, S., Kamizuka, T., Hirota, T., et al. 2019, ApJL, 875, L29, doi: 10.3847/2041-8213/ab1653

Tanaka, K. E. I., Zhang, Y., Hirota, T., et al. 2020, ApJL, 900, L2, doi: 10.3847/2041-8213/abadfc

The Astropy Collaboration, Price-Whelan, A. M., Lian Lim, P., et al. 2022, arXiv e-prints, arXiv:2206.14220. https://arxiv.org/abs/2206.14220 van der Walt, S., Colbert, S. C., & Varoquaux, G. 2011, Computing in Science and Engineering, 13, 22, doi: 10.1109/MCSE.2011.37

Virtanen, P., Gommers, R., Oliphant, T. E., et al. 2020, Nature Methods, 17, 261, doi: 10.1038/s41592-019-0686-2

Whitaker, J. S., Jackson, J. M., Rathborne, J. M., et al. 2017, AJ, 154, 140, doi: 10.3847/1538-3881/aa86ad

Woitke, P., Helling, C., Hunter, G. H., et al. 2018, A&A, 614, A1, doi: 10.1051/0004-6361/201732193

Xu, Y., Moscadelli, L., Reid, M. J., et al. 2011, ApJ, 733, 25, doi: 10.1088/0004-637X/733/1/25

Zinchenko, I., Liu, S. Y., Su, Y. N., et al. 2015, ApJ, 810, 10, doi: 10.1088/0004-637X/810/1/10

Zinchenko, I. I., Liu, S.-Y., Su, Y.-N., Wang, K.-S., & Wang, Y. 2020, ApJ, 889, 43, doi: 10.3847/1538-4357/ab5c18

APPENDIX

A. ADDITIONAL FIGURES FOR SALTED SOURCES

For the salted sources, we present moment maps and spectra with lines identified in the following Appendices.

A.1. *G351.77mm1*

We show additional moment maps, spectra, and position-velocity diagrams from G351.77mm1 in this section. This object is one of the most compelling, high signal-to-noise objects in the sample, yet its kinematics are perplexing, exhibiting disk-like rotation in the same direction as the larger-scale outflow rather than rotating perpendicular to the outflow, as we would expect. Figure 12 shows the stacked spectra. Figure 8 shows moment-0 and moment-1 maps of NaCl and H_2O. Figure 13 shows the same for SiS and PN. All four molecules exhibit similar morphology and kinematics, including a prominent central hole, which is strongly suggestive of a disk. Figure 14 shows moment-0 maps and position-velocity diagrams, and Figure 15 more position-velocity diagrams, illustrating that rotation is a plausible explanation for the observed kinematics.

A.2. *G351.77mm2*

Figure 16 shows the stacked spectra of G351 mm2. Figure 17 shows the moment-0 and moment-1 maps of NaCl and H_2O, which are only marginally resolved.

A.3. *G351.77mm12*

Figure 18 shows the stacked spectra of G351 mm12. This source is unresolved, as shown in Fig 2. Figure 19 shows the moment-0 and moment-1 maps of NaCl and H_2O, which are only marginally resolved.

A.4. *NGC6334I*

We show additional figures of NGC6334I, including spectra (Fig 20 and moment maps (Fig 21. For mm2b, we show only the stacked spectrum (Fig 22), since the source is unresolved

A.5. *W33A*

The labeled, stacked spectrum from W33A is shown in Figure 23. The four-panel moment map is not shown for this source because it is unresolved and shows no structure; it is consistent with a point source.

A.6. *I16547A*

The labeled, stacked spectrum from I16547A is shown in Figure 24. Moment-0 and moment-1 images are shown in Figure 25. A position-velocity diagram, with overlaid Keplerian curves for an edge-on orbit with masses labeled, is shown in Figure 28. We show these to provide order-of-magnitude mass estimates, but note that we have no constraint on the disk inclination and have not attempted to model the extent of the disk emission. No outflow is observed toward A (Tanaka et al. 2020).

A.7. *I16547B*

The labeled, stacked spectrum from I16547B is shown in Figure 26. Moment-0 and moment-1 images are shown in Figure 27. A position-velocity diagram, with overlaid Keplerian curves for an edge-on orbit with masses labeled, is shown in Figure 28. We show these to provide order-of-magnitude mass estimates, but note that we have no constraint on the disk inclination and have not attempted to model the extent of the disk emission. An SiO outflow is observed toward B, perpendicular to the gradient in the PV diagram (Tanaka et al. 2020).

A.8. *Continuum*

We show Figures 1 and 2 again, but this time with continuum contours overlaid, in Figures 29 and 30.

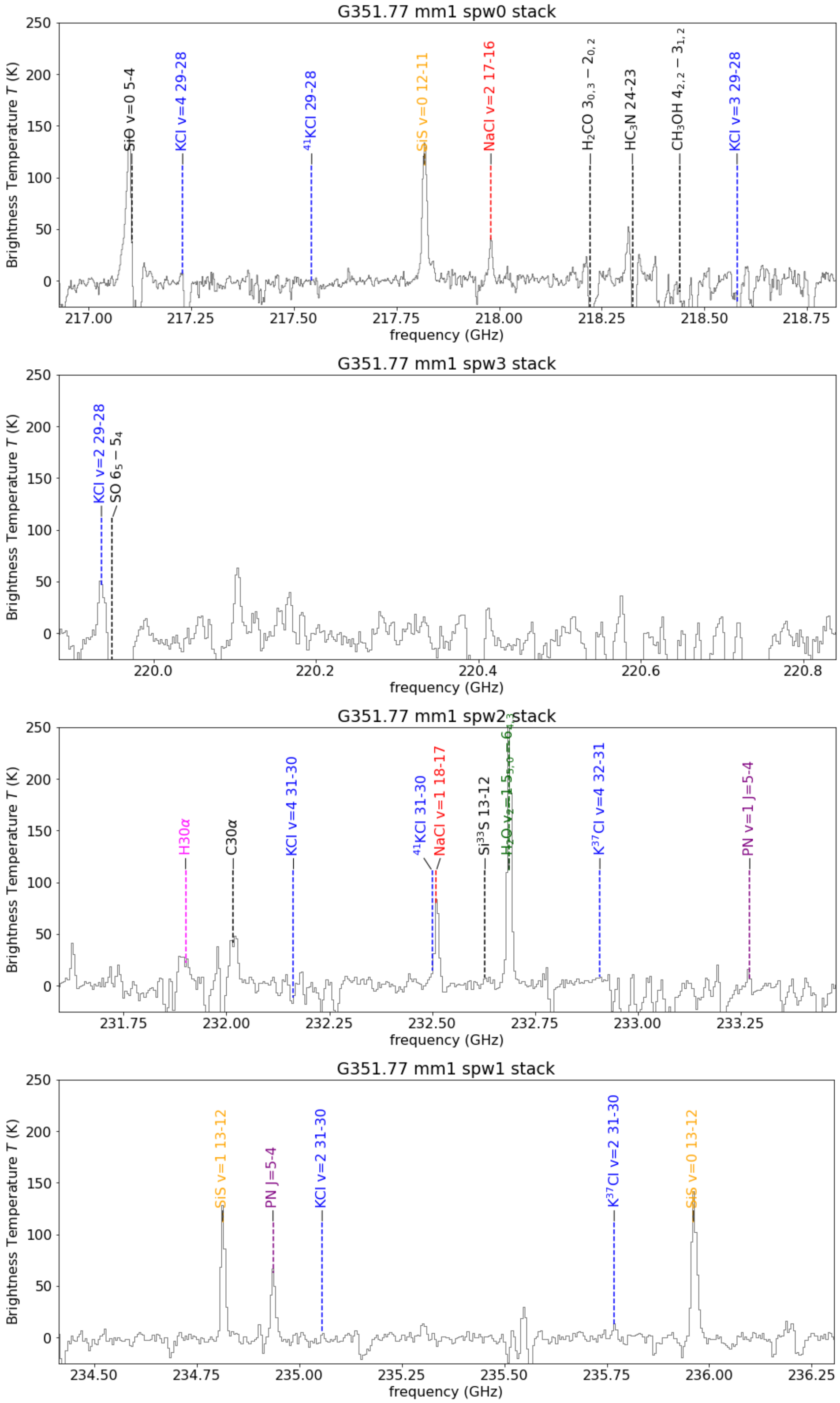

Figure 12. Stacked spectra from G351.77mm1 from the Beuther et al. (2019) data set. The stacking was based on the H_2O line. Line IDs are shown; no KCl detections are clear. Different colors are used for targeted species with multiple transitions in-band: orange for SiS, blue for KCl, red for NaCl, magenta for H30α, purple for PN, and green for H_2O. The remaining species, with only one transition marked, are shown in black. The PN line identification should be taken with a grain of salt since it is the only transition we observe from PN.

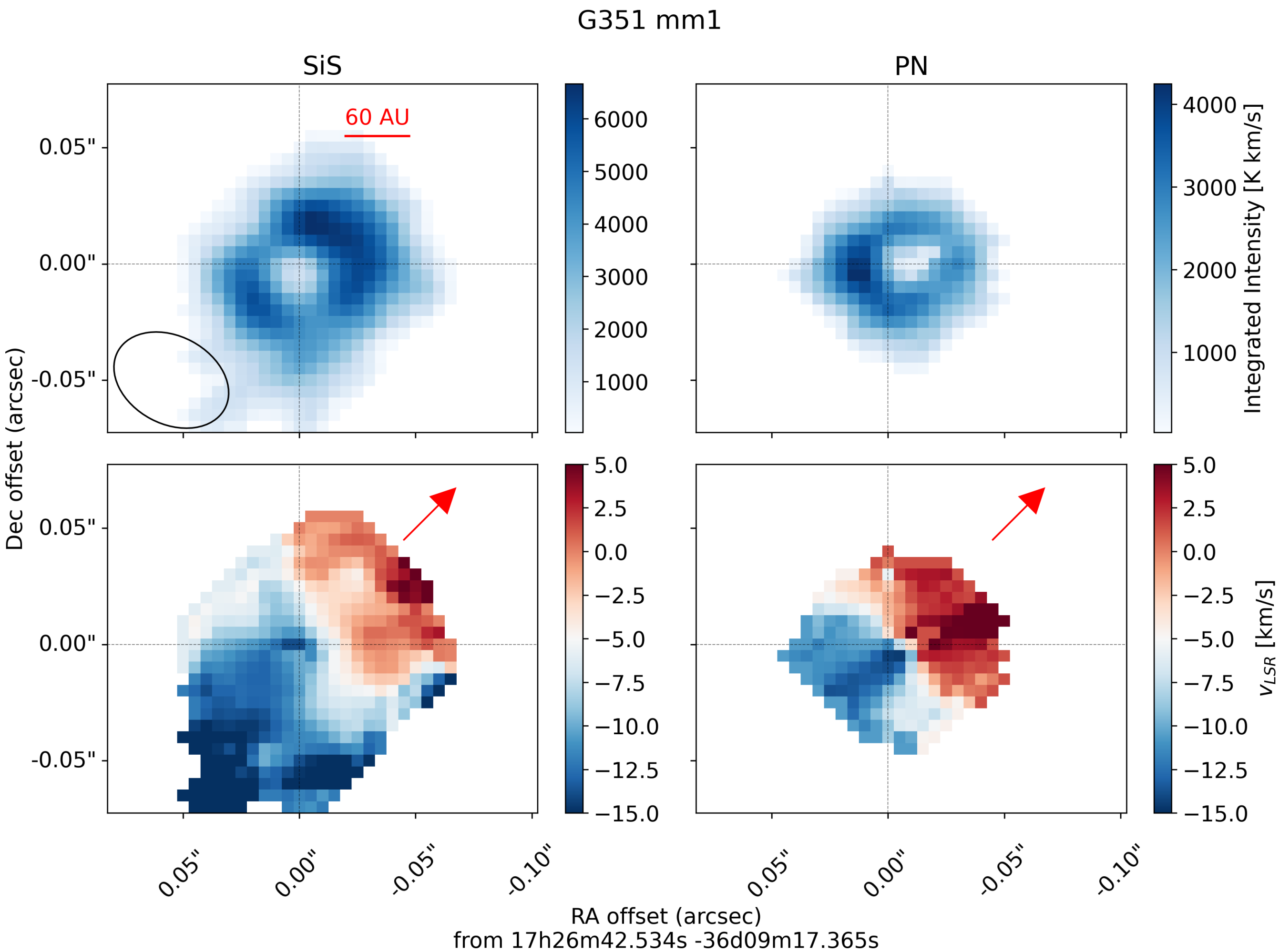

Figure 13. Moment-0 and 1 images as in Figure 8, but for the SiS v=0 J=13-12 and PN 5-4 lines of G351 mm1.

B. UNSALTED SOURCES

B.1. *I16562*

IRAS16562-3959 is also known as G345.4938+01.4677. This source shows SO in absorption against a continuum disk. It exhibits RRL emission that shows a very tiny gradient; Guzmán et al. (2020) reported the detection of an ionized disk in this system based on RRL emission. No other emission lines are associated with the RRL possible disk. There is extensive CH_3CN emission around this source with kinematics more complicated than a simple Keplerian disk.

B.2. *G333*

We adopt naming from Stephens et al. (2015), though their resolution was only $\sim 2.5''$.

G333.23mm1 is the bright central region. Morphologically, it looks like the hub at the center of several converging filaments. There is no obvious sign of a disk in any of the lines we examined. There is no hint of brinary lines.

G333.23mm2 shows some sign of a line gradient in CH_3OH, hinting that a disk is present. However, no brinary lines are seen.

B.3. *G335*

Olguin et al. (2022) performed an extensive study of this system using the data presented here. G335-ALMA1 is the bright central source that shows signs of rotation, but no clear disk. Instead, it appears dominated by inflowing

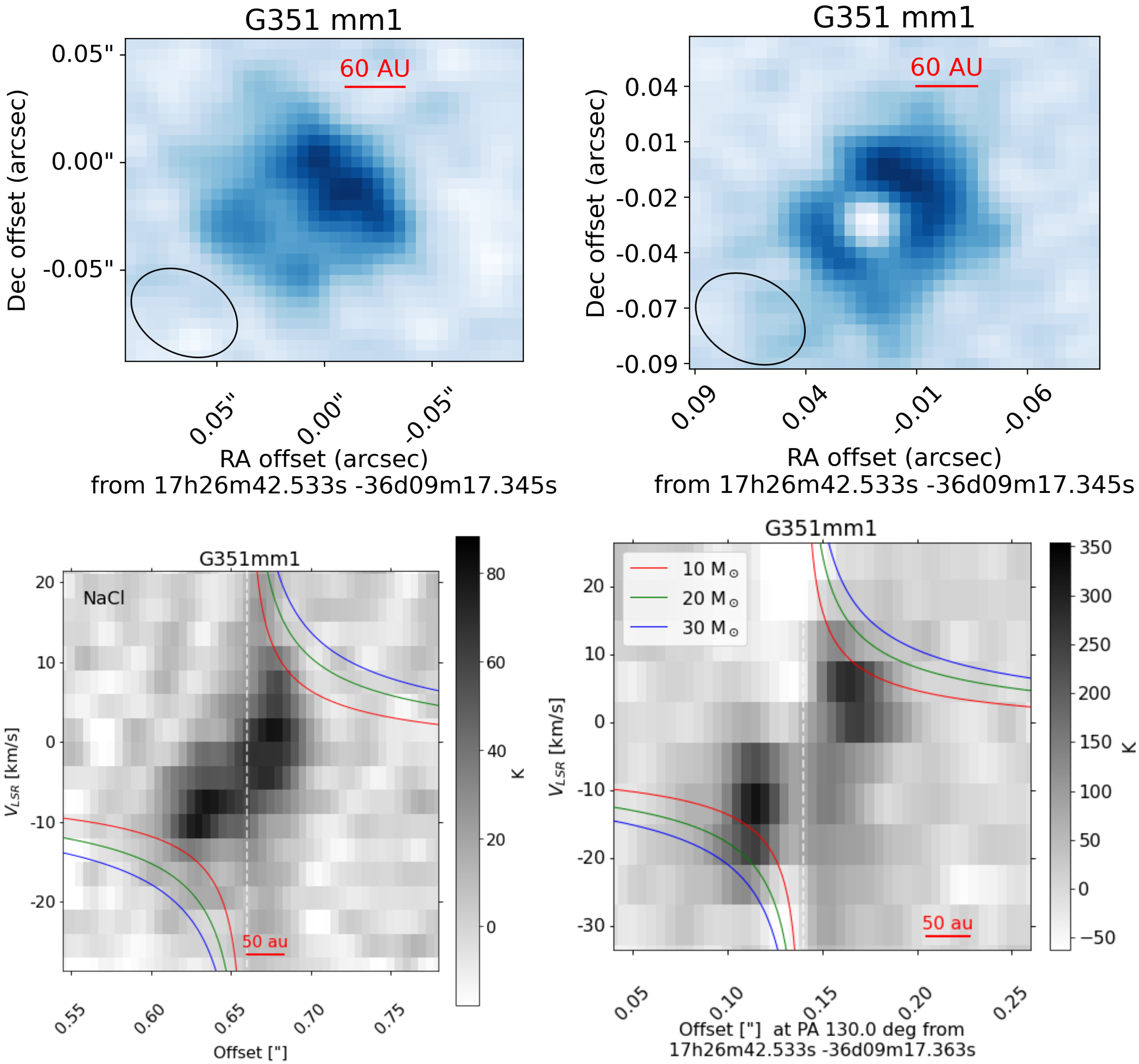

Figure 14. Comparison of NaCl and SiS moment-0 and position-velocity maps of G351.77mm1. (top left) NaCl stack moment 0 image, as seen in Figure 1. (top right) SiS 13-12 moment 0 image, showing similar morphology. (bottom left) NaCl stack cube position-velocity diagram extracted along the direction of maximum gradient. (bottom right) SiS 13-12 position-velocity diagram extracted along the direction of maximum gradient. Keplerian rotation curves assuming an edge-on central source with the listed mass are shown in colored lines; these curves are not fits to the data and do not account for inclination, they are just provided to guide the eye. Furthermore, as discussed in Section 3.3.2, the velocity gradient shown here may trace an outflow rather than a disk.

accretion filaments. The spectrum is extremely rich, and we adopt the same CH_3OH line as in Olguin et al. (2022) as our velocity reference. No brinary lines are detected.

B.4. *G5.89*

The G5.89 image is dominated by an extended HII region. The only disklike source in the imaged field of view is mm15, so our cutout centered on that source. It apparently exhibits *no* line emission at all in the present data set. We examined the other millimeter peaks in the region, but found no obvious signatures of disks or brinary lines.

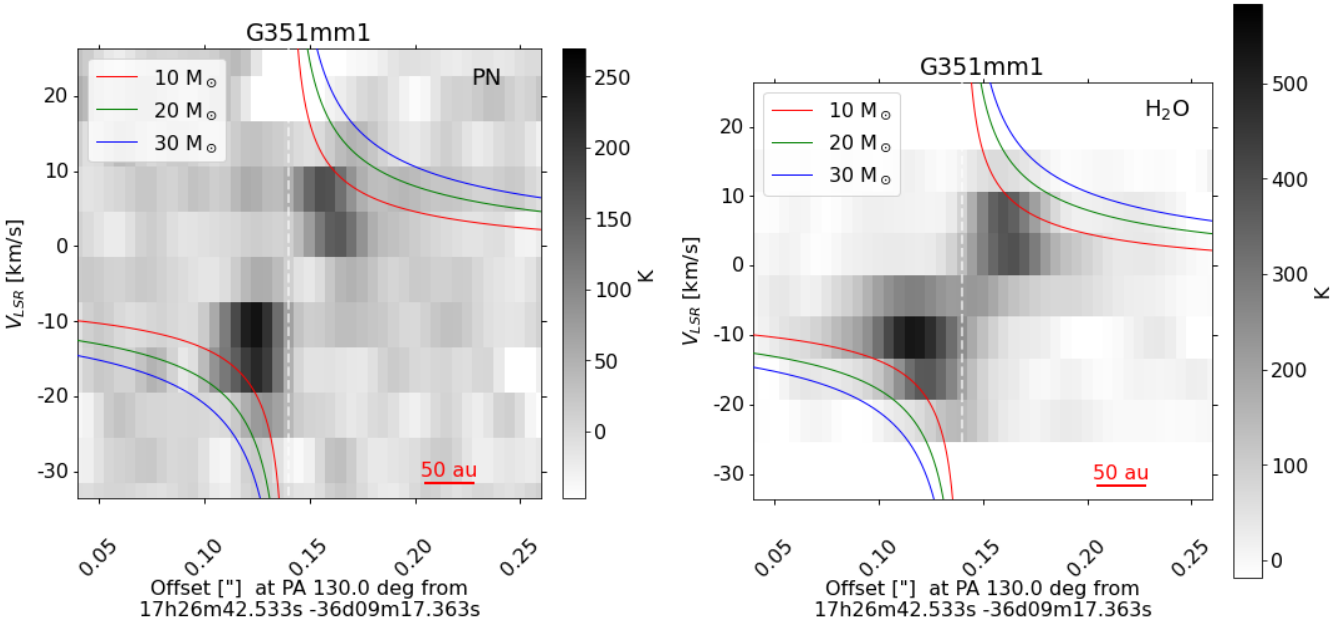

Figure 15. Two more position-velocity diagrams of G351 mm1, showing the 235 GHz PN 5-4 line (newly identified here) and the H_2O line. The common structure seen in these diagrams, and in Figure 14, justifies our assumption that these have common kinematics. Keplerian rotation curves assuming an edge-on central source with the listed mass are shown in colored lines; these curves are not fits to the data and do not account for inclination, they are just provided to guide the eye. Furthermore, the direction of maximum gradient, along which these diagrams are extracted, points in the direction of the outflow.

B.5. *GGD27*

GGD27mm1 (otherwise referred to here as GGD27) is the driving source of HH80/81 (Girart et al. 2017, 2018; Añez-López et al. 2020). It is also known as IRAS 18162-2048. It has a clear, well-defined, massive ($M \sim 5 M_\odot$) disk orbiting a $\sim 20\ M_\odot$ star (Añez-López et al. 2020). There is no sign of NaCl, H_2O, KCl, or SiS in the spectrum of the disk in our data or previous observations (Girart et al. 2017). It is bright in SO $6_5 - 5_4$, which we used to stack spectra to perform a deeper search.

This source is the archetype of non-salt-bearing disks. Its well-defined Keplerian line profiles, high central mass, and line-poor spectrum demonstrate that not all HMYSO disks exhibit salt emission. The system is very similar to SrcI in terms of its central stellar mass, disk size (though GGD27's is 2-4× larger in radius), and luminosity, suggesting that none of these features are critical for releasing salt into the gas phase. As the driver of the HH80/81 outflow, it is also clear that the simple presence of an outflow does not determine whether brinary lines are produced. However, one notable difference is that the HH80/81 jet is highly collimated (Rodríguez-Kamenetzky et al. 2017; Qiu et al. 2019), while SrcI drives a broader disk wind (Hirota et al. 2017; Tachibana et al. 2019), hinting that the driving mechanism of the outflow may have a role in determining when salts are detectable. The comparison of this source to SrcI and others in this sample will be useful for future understanding of the origin of salts.

B.6. *IRAS18089*

Sanhueza et al. (2021) observed this source at high resolution, though they focused on the magnetic field. Previously, Beuther et al. (2004, 2005) showed that this source was line-rich with SMA observations. We used a CH_3OH as the stacking line because the kinematics were similar across all bright lines, including the SO $6_5 - 5_4$ line, but the SO line was affected by strong absorption toward the inner disk. The line kinematics were reasonably disk-like, but not consistent with a single Keplerian disk; the velocity structure in this source requires more sophisticated modeling. Nevertheless, there is no sign of brinary lines in the averaged or stacked spectra.

B.7. *G34.43mm1*

There is a structure toward the center of G34.43mm1 with a clear line gradient, but it does not trace disk-like kinematics and is quite extended. On the larger scale, G34.43mm1 drives a powerful outflow (Sanhueza et al. 2010).

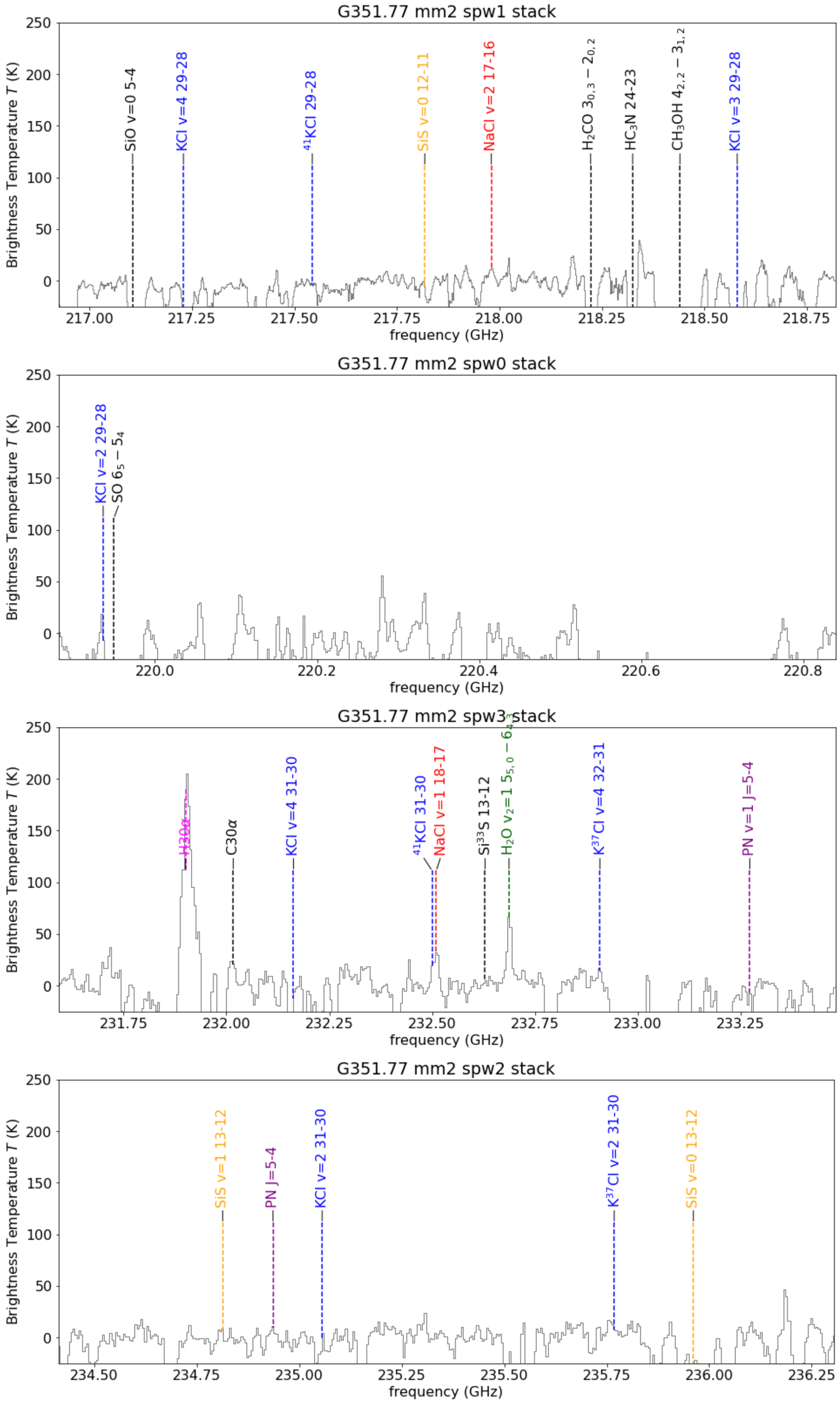

Figure 16. The G351 mm2 disk candidate stacked spectrum. Like mm1 (Fig. 12), the stacking was done on the H_2O line. However, other lines are at most weakly detected; the NaCl v=1 J=18-17 line is evident, but no other clear detections are present in this or other bands. In all spectra, but particularly in spectral window 0, much of the spectrum is absorbed by material unassociated with the disk; we cut off the absorption features to emphasize emission features here.

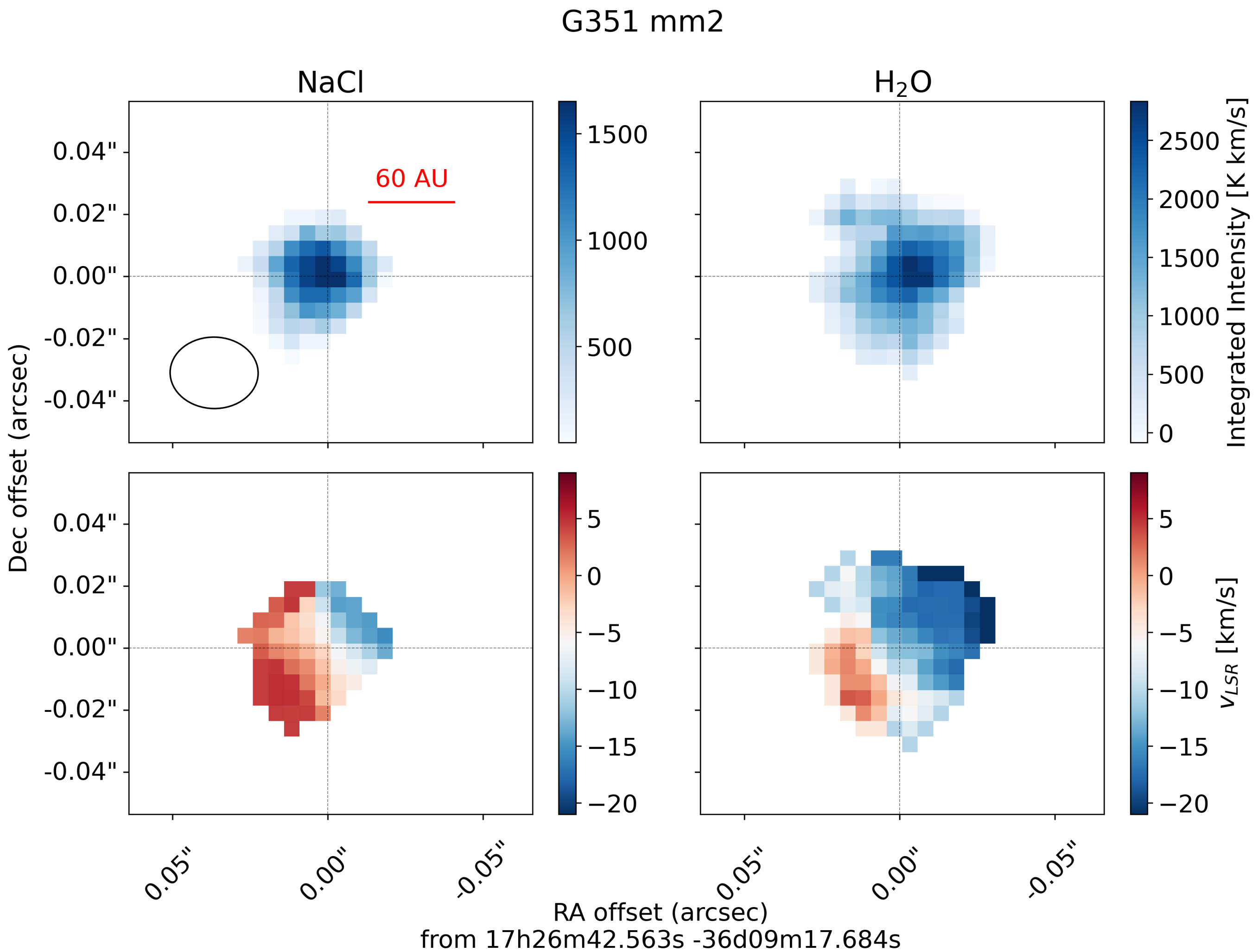

Figure 17. Moment-0 (integrated intensity) and moment-1 (intensity-weighted velocity) images of stacked NaCl (left) and H_2O (right) for G351 mm2.

While this is region is quite nearby (1.56 kpc Xu et al. 2011), it is not among the salt-bearing candidates. Despite its relatively near distance, the observed spatial resolution is only $\sim$ 400 au, which is much larger than the detected disks. The overall appearance of the inner region suggests that streamers are feeding in to a central region. The chemically rich inflowing material results in a very spectrally dense spectrum (e.g., Sanhueza et al. 2012; Liu et al. 2020a), which likely prevents detection of brinary features even if they are present. This is a good candidate for followup at higher angular resolution.

B.8. *G29.96*

Beuther et al. (2007) and Beltrán et al. (2011) studied this region at $\sim$arcsecond resolution. The target region is centered on the brightest few sources at the center. The distance to this object is unclear, with Beltrán et al. (2011) reporting 3.5 kpc and Kalcheva et al. (2018) reporting 7.4 kpc. There is no clear signature of any of the lines of interest, nor is there a clear signature of rotation. There is a tentative detection of SiS v=0 12-11, but neither of the SiS v=1 lines (13-12 or 12-11) appear, so this detection is uncertain.

B.9. *S255IR*

Sh 2-255 IR SMA1 (S255IR) was the recent (< 10 years) site of a major accretion outburst. As such it is a strong candidate for being actively heated over its 'normal' level.

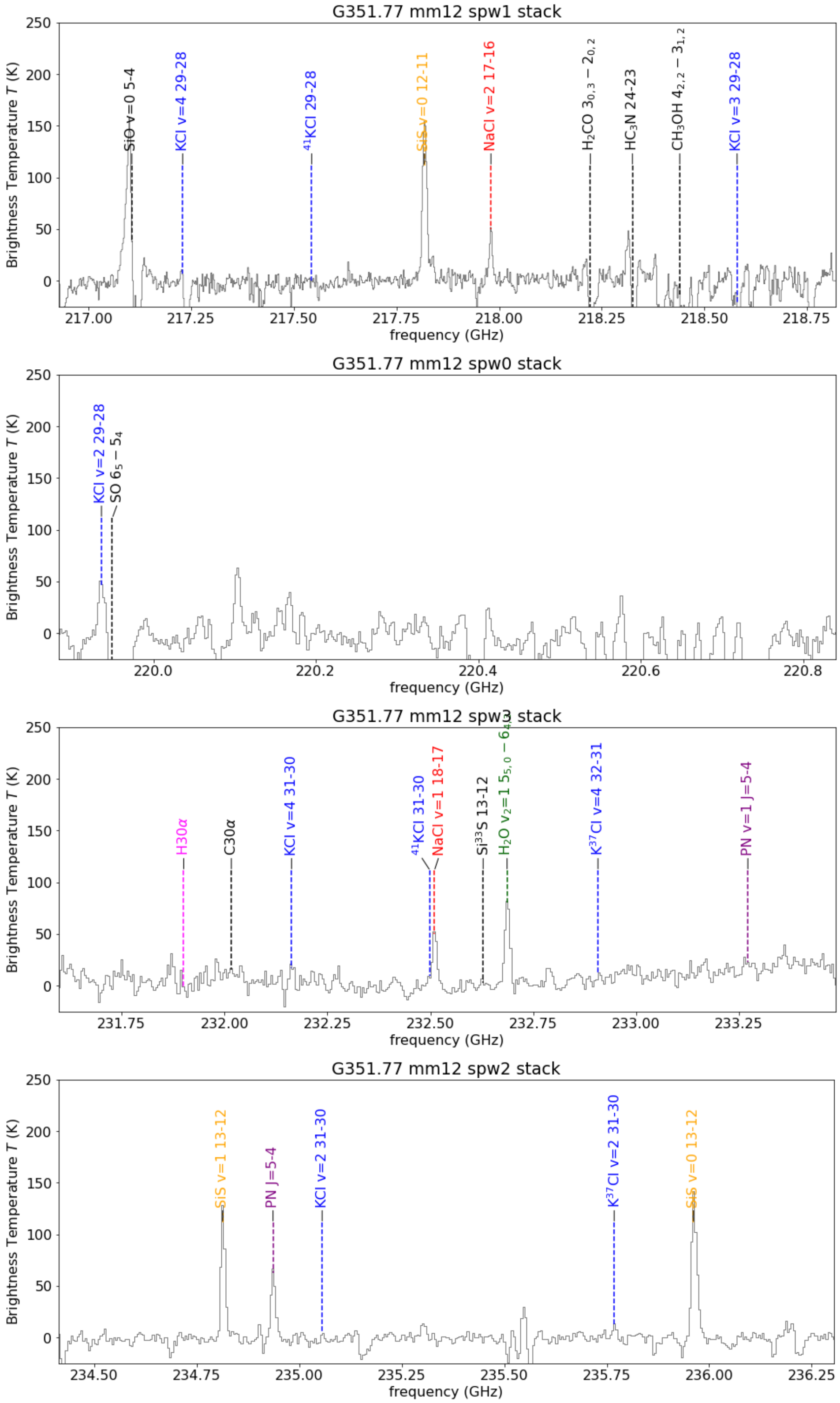

Figure 18. The G351 mm12 disk candidate stacked spectrum. See Figure 12 for additional description.

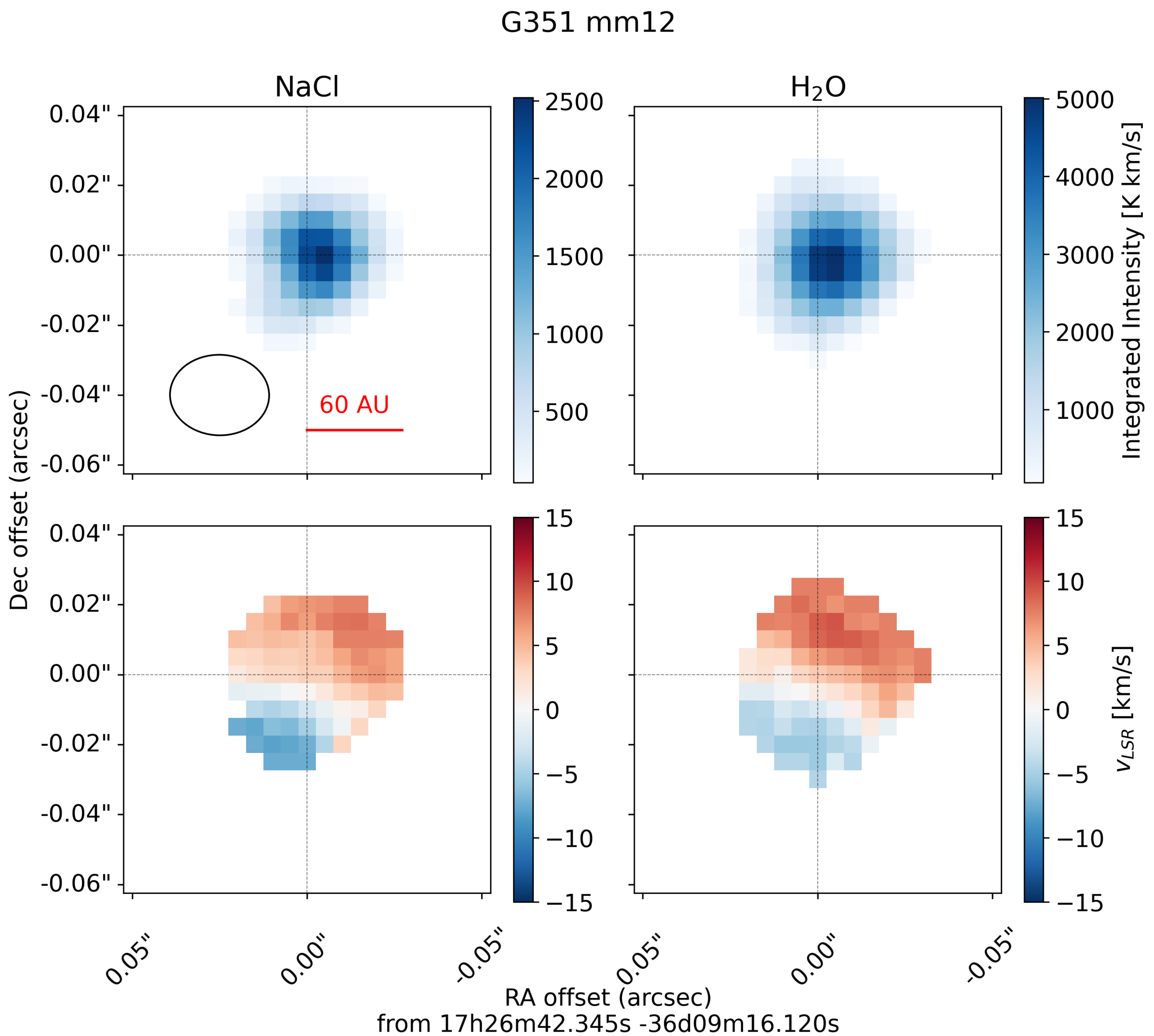

Figure 19. Moment-0 (integrated intensity) and moment-1 (intensity-weighted velocity) images of stacked NaCl (left) and H_2O (right) for G351 mm12.

No disk is obvious in the data cube from rotational signatures. While several authors (Zinchenko et al. 2015, 2020; Liu et al. 2020b) have noted bulk rotation in the molecular gas around S255IR, these signatures are not evident on the smaller ($\sim$ 70 au) scales probed here.

There is, however, a hint of both H_2O and H30α emission along the innermost part of the outflow, within about one resolution element of the central source. There is also a hint of SiS here. There is clearly SiO emission with a velocity gradient along the outflow axis, but curiously it is not very bright along the continuum jet. This source warrants followup at higher resolution and sensitivity to try to identify the location of the actual disk, though it is not yet clear which lines to use for this search.

B.10. *NGC6334IN*

The NGC6334IN region contains several bright sources. The brightest in our observations are SMA6 and SMA1 b/d (names from Sadaghiani et al. 2020). Neither source shows clear signs of rotation in any line. SMA1b/d contains

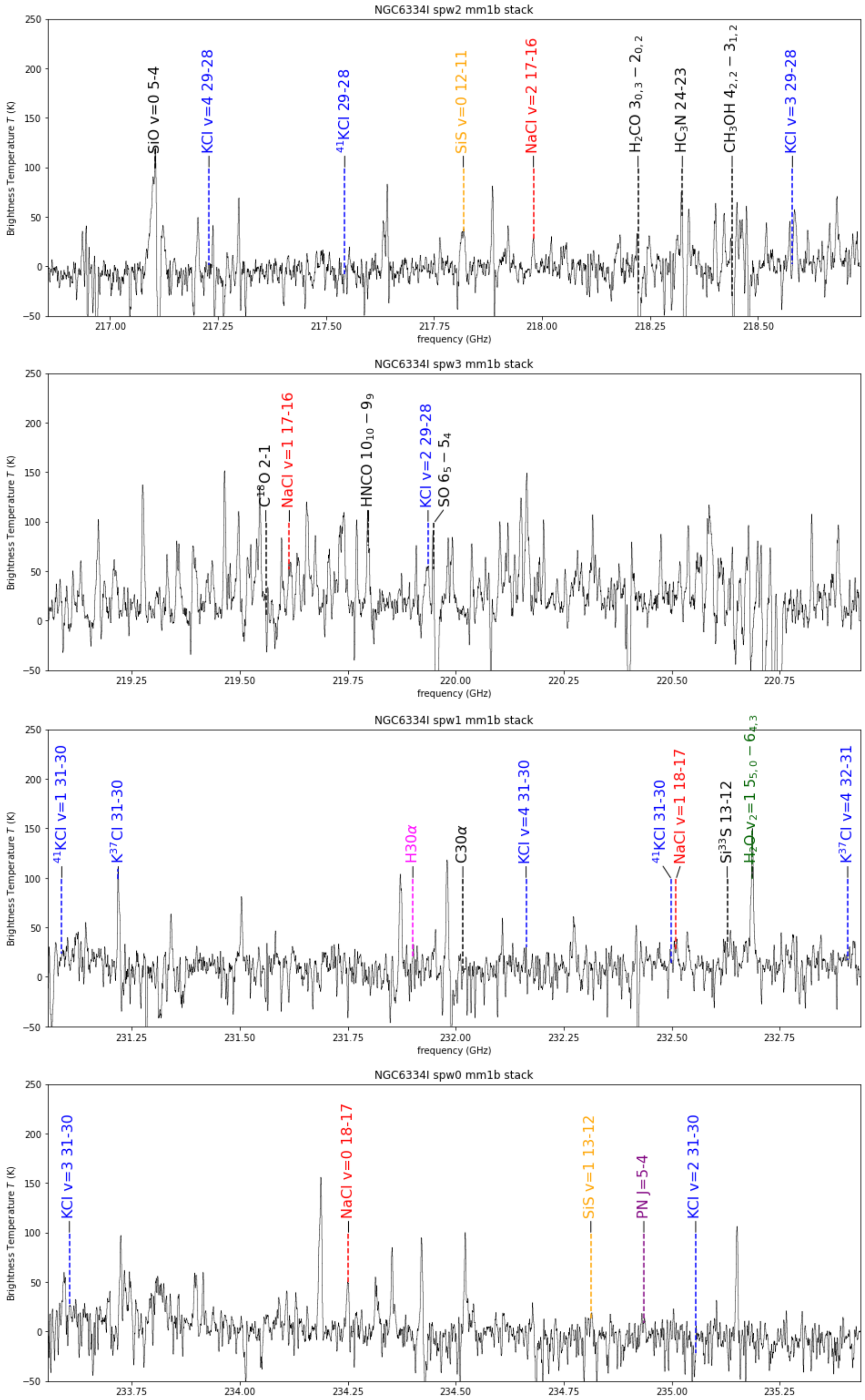

Figure 20. The NGC6334I mm1b disk stacked spectrum. See Figure 12 for additional description.

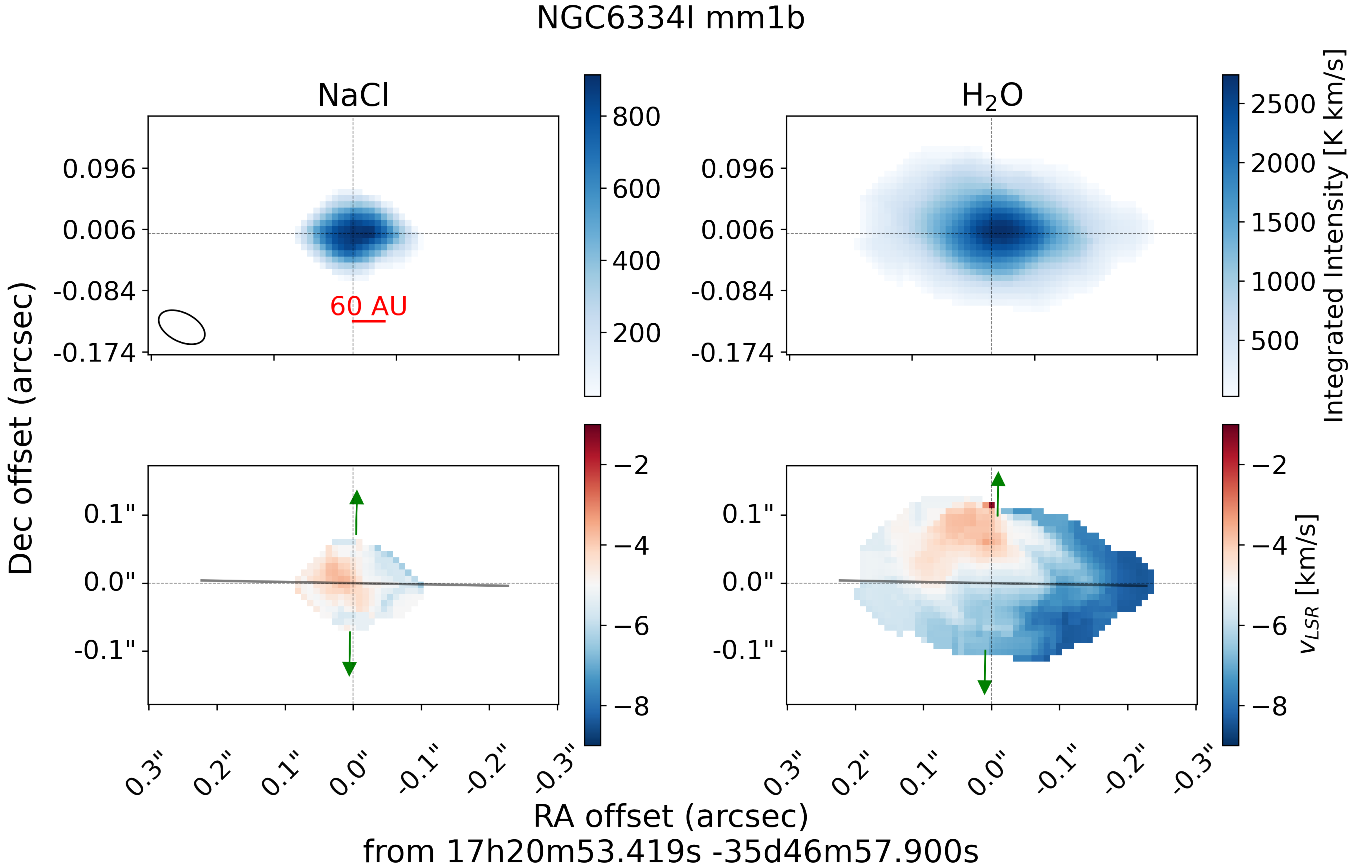

Figure 21. Moment-0 and 1 images as in Figure 8, but for NGC 6334I mm1b. The outflow noted by Brogan et al. (2018) is shown at PA=-5° with green arrows, as it appears to be primarily in the plane of the sky. The solid gray line shows the orientation from which the position-velocity diagram (Figure 9) is extracted.

several sources that may exhibit some hint of H_2O emission, so we use that line as the basis for stacking We do not detect any other lines. Notably, both SO and SiO appear absent toward these sources. SMA6 also shows a hint of a water line, but similarly shows no sign of any of the other targeted lines.

B.11. *G11.92mm1*

Ilee et al. (2018) reported on the disk G11.92mm1, showing a much larger ($r \sim 800$ au) size than most of the sources in our sample. We use SO $6_5 - 5_4$ as the guide line for stacking, since it shows clear disk kinematics. No brinary lines are detected.

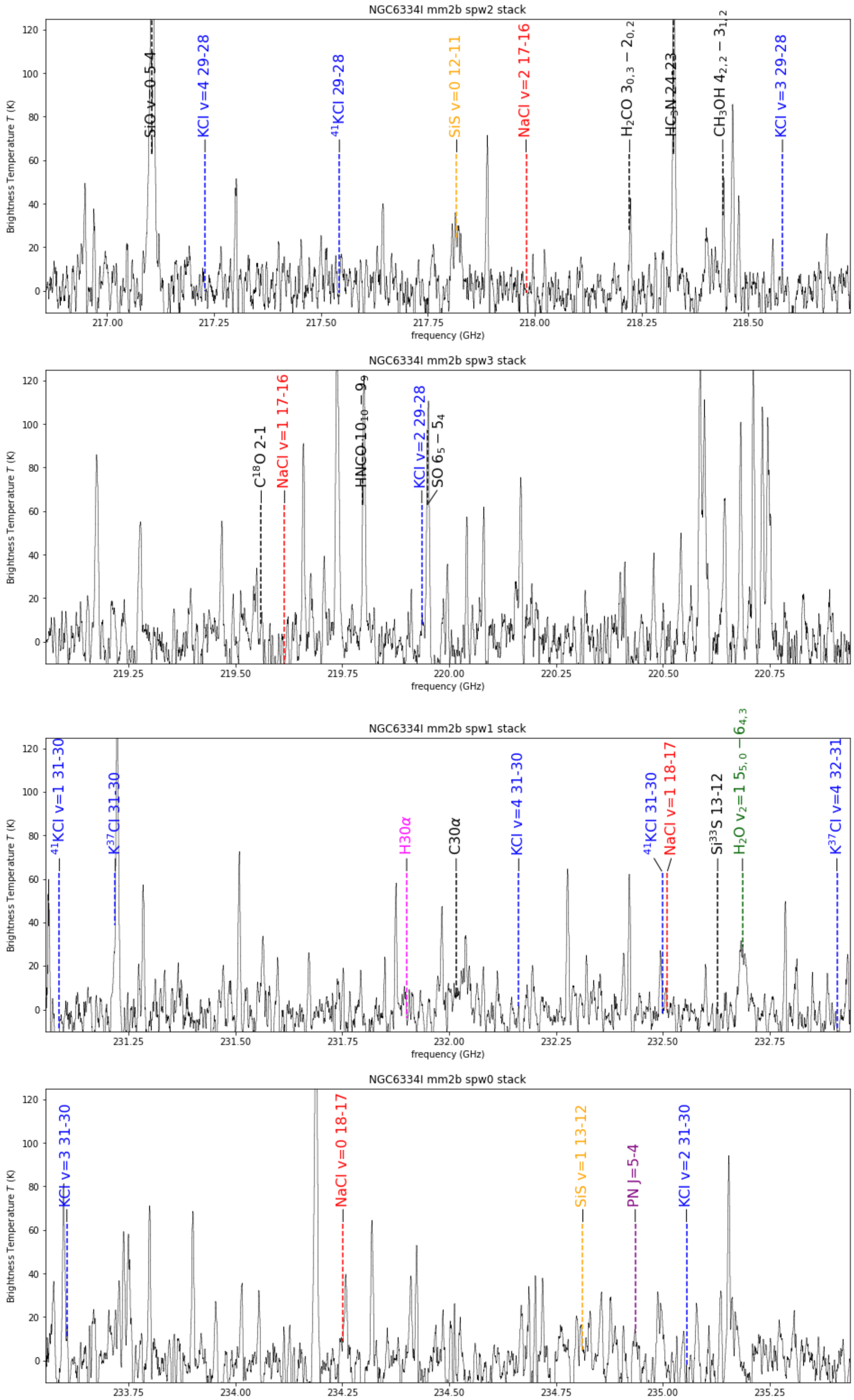

Figure 22. The NGC6334I mm2b disk stacked spectrum. See Figure 12 for additional description.

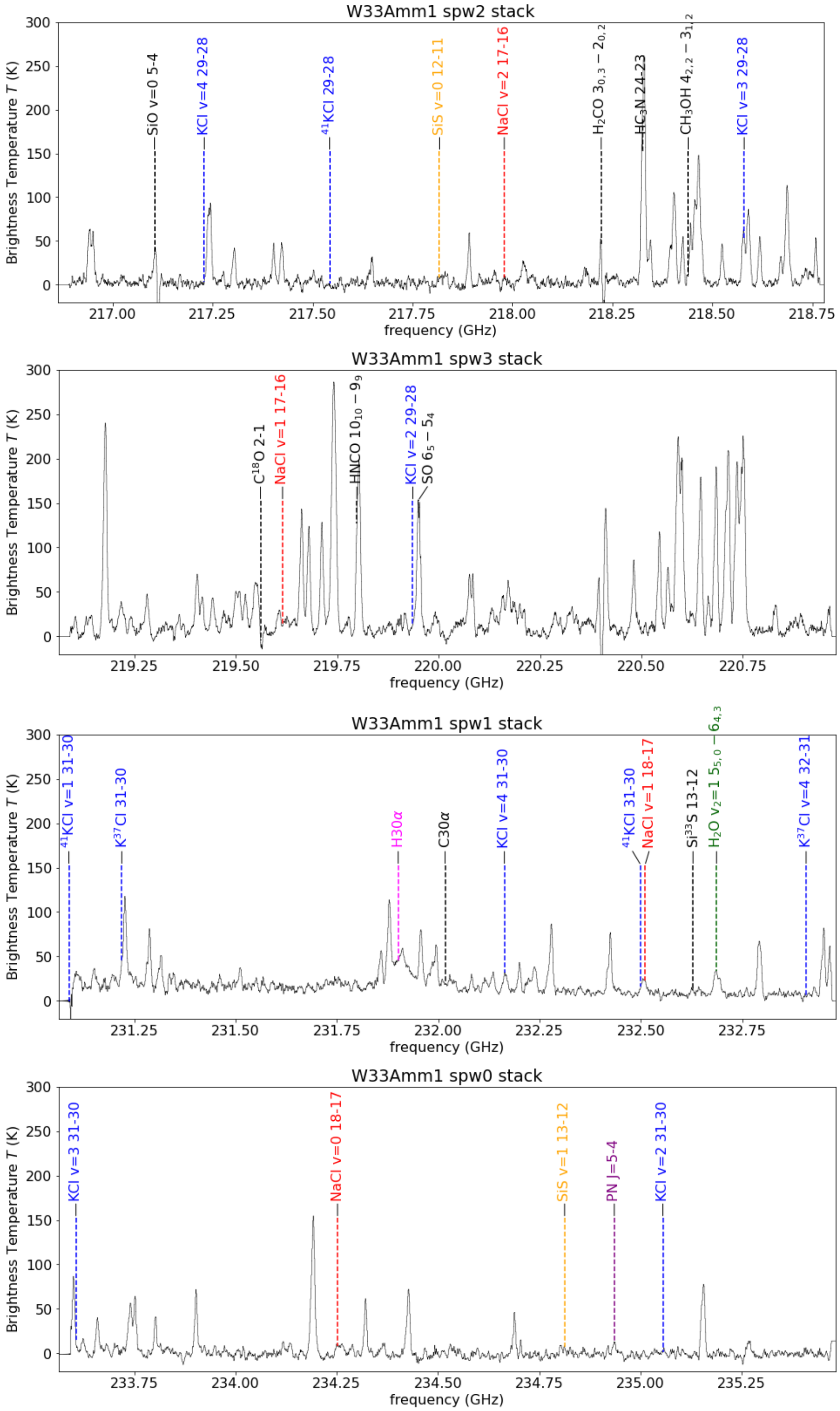

Figure 23. The W33A disk stacked spectrum. See Figure 12 for additional description.

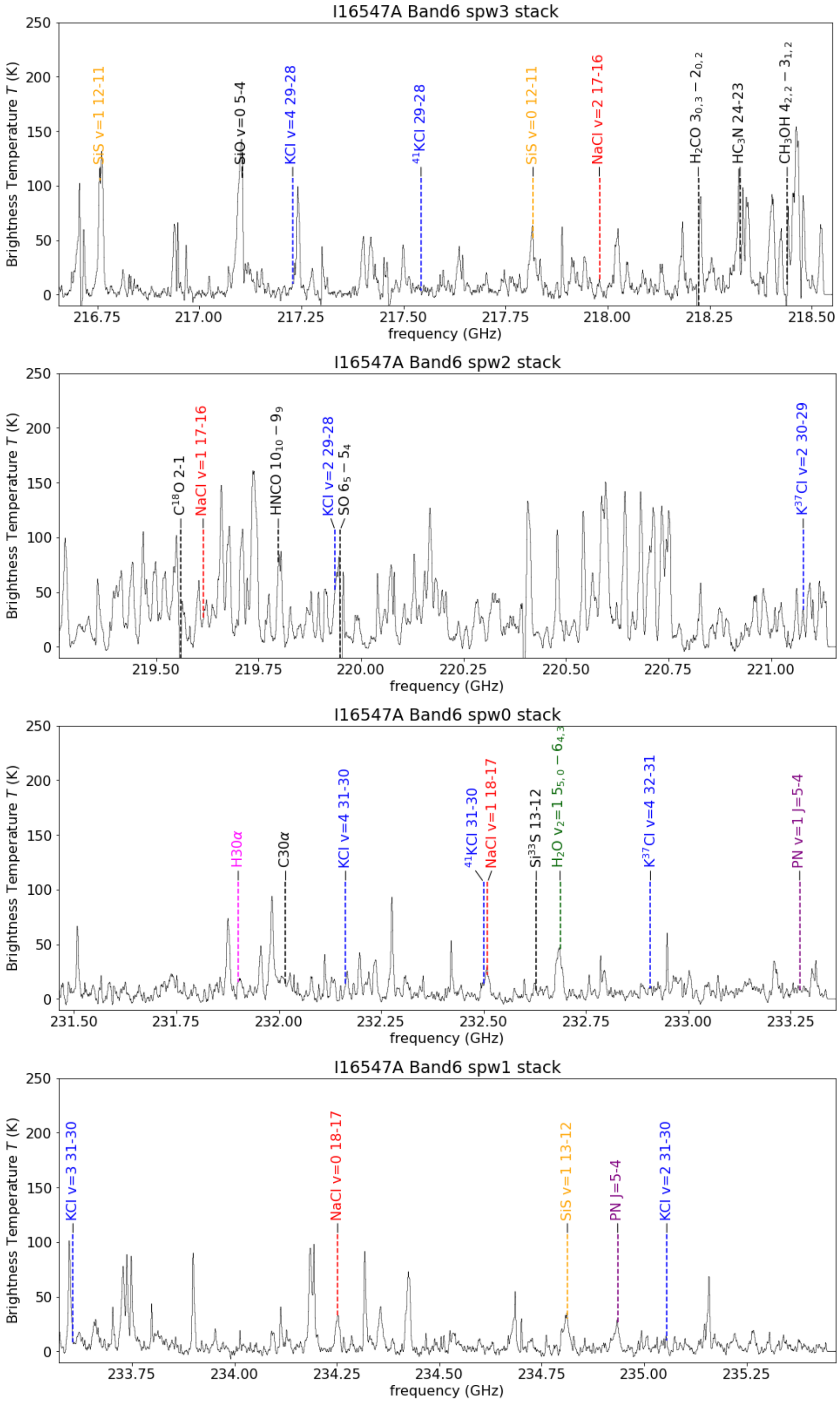

Figure 24. The I16547A disk stacked spectrum. See Figure 12 for additional description.

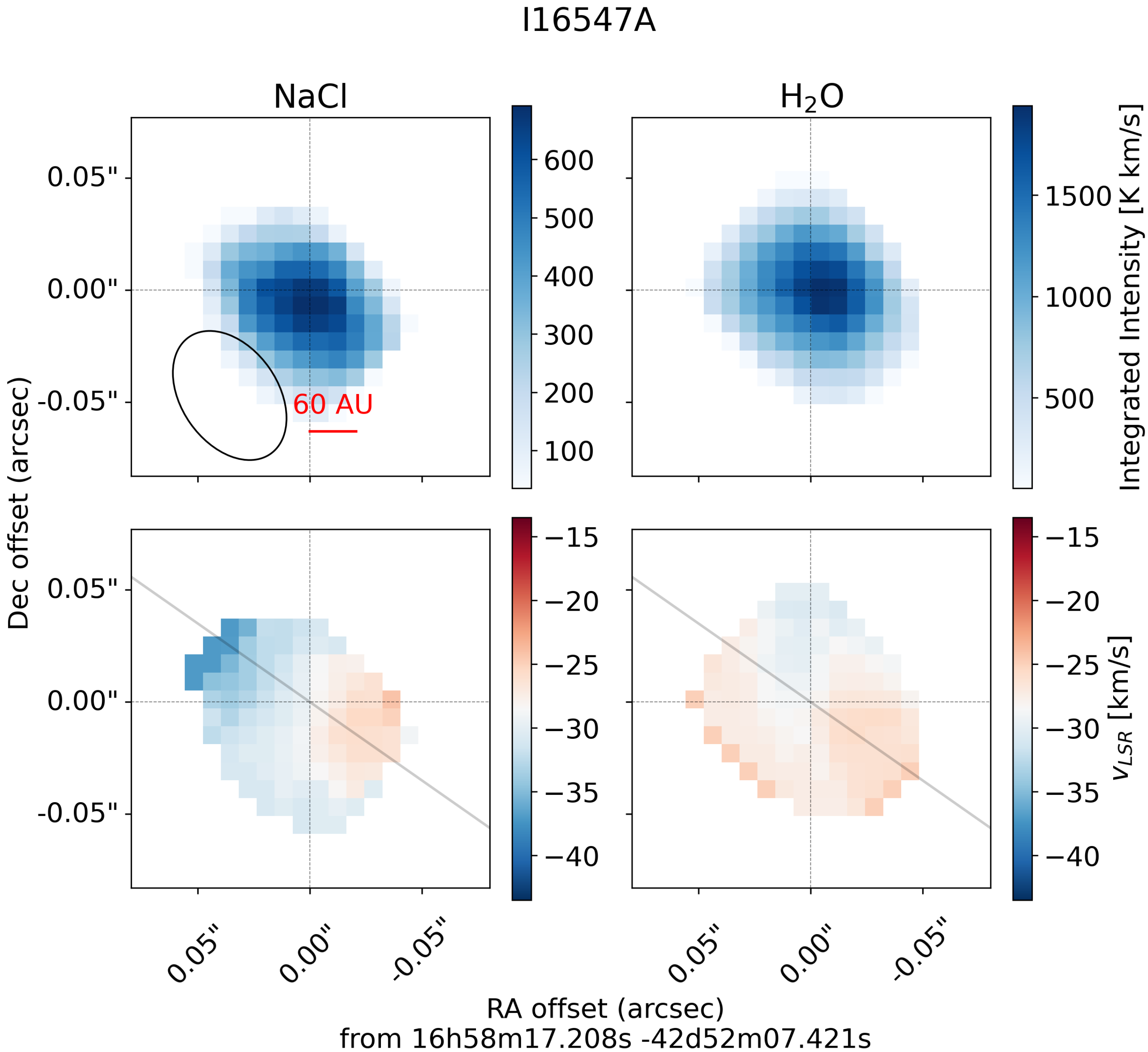

Figure 25. Moment-0 and 1 images as in Figure 8, but for IRAS 16547A The solid gray line shows the orientation from which the position-velocity diagram (Figure 28) is extracted, based on the angle determined in Tanaka et al. (2020). The radio jet at PA=-16° is shown with arrows (Tanaka et al. 2020).

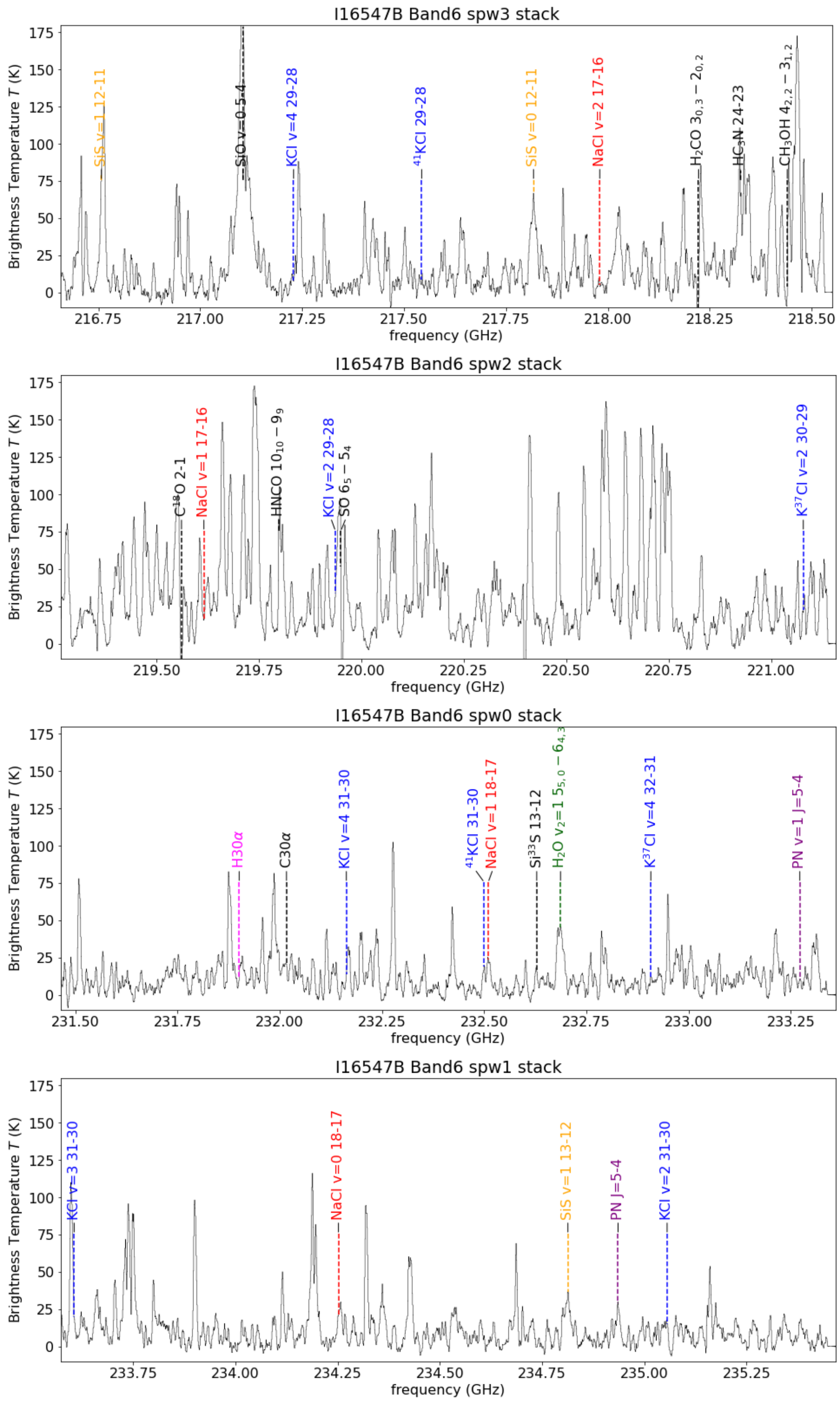

Figure 26. The I16547B disk stacked spectrum. See Figure 12 for additional description.

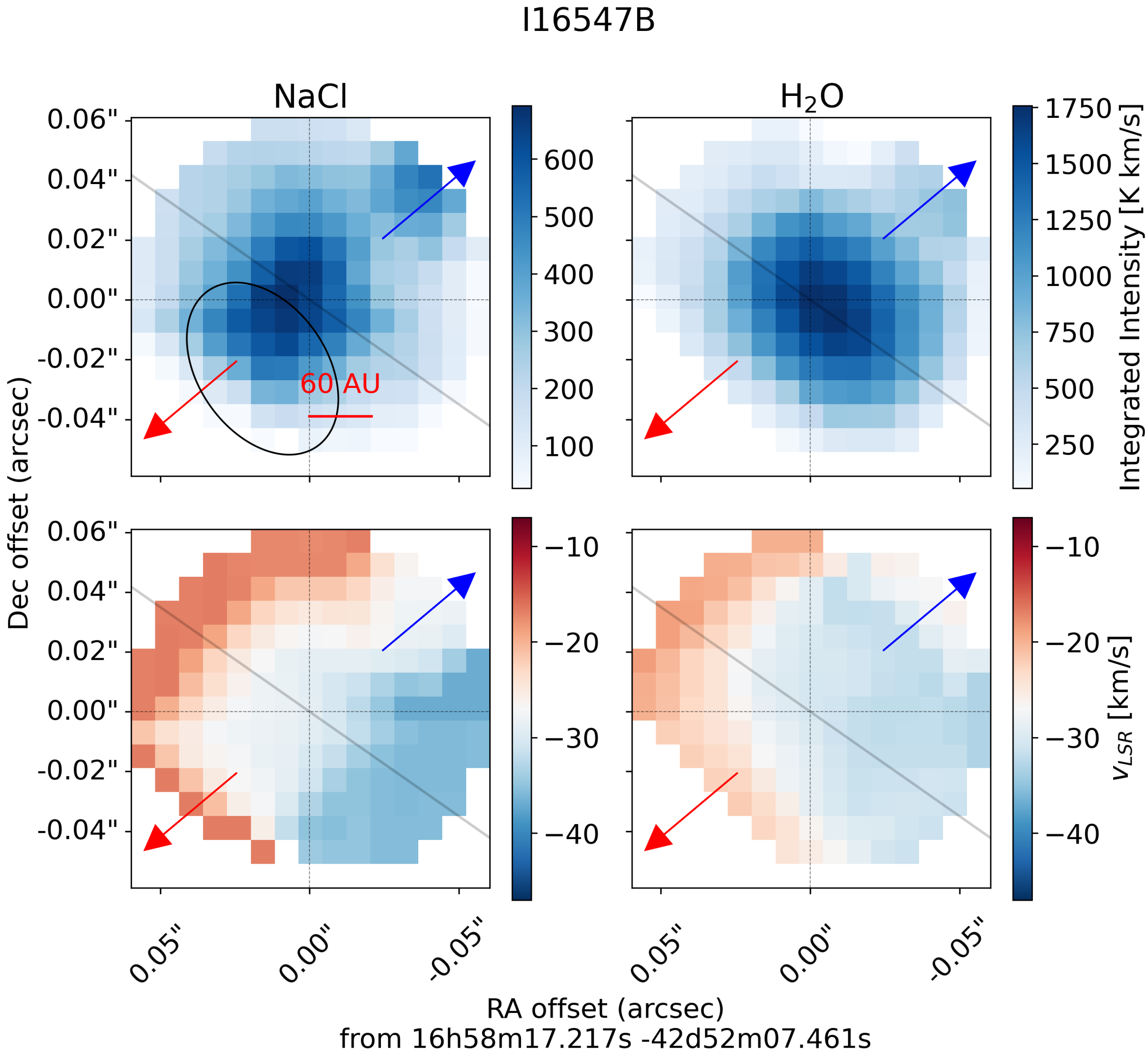

Figure 27. Moment-0 and 1 images as in Figure 8, but for IRAS 16547B The solid gray line shows the orientation from which the position-velocity diagram (Figure 28) is extracted, based on the angle determined in Tanaka et al. (2020). The red and blue arrows indicate the direction of the SiO outflow noted in Tanaka et al. (2020).

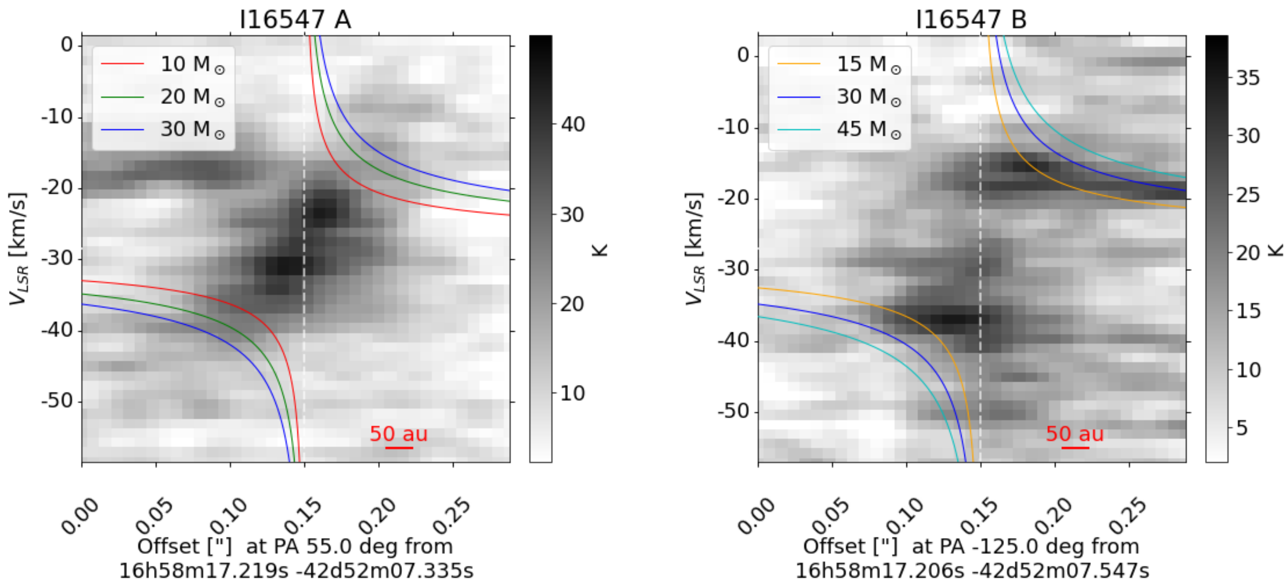

Figure 28. Position-velocity diagrams of the I16547 disks in the stacked NaCl lines. The overplotted curves show Keplerian rotation around central point sources with masses indicated in the caption, assuming an edge-on inclination. As noted in Tanaka et al. (2020), the disks appear to be counter-rotating along similar position angles.

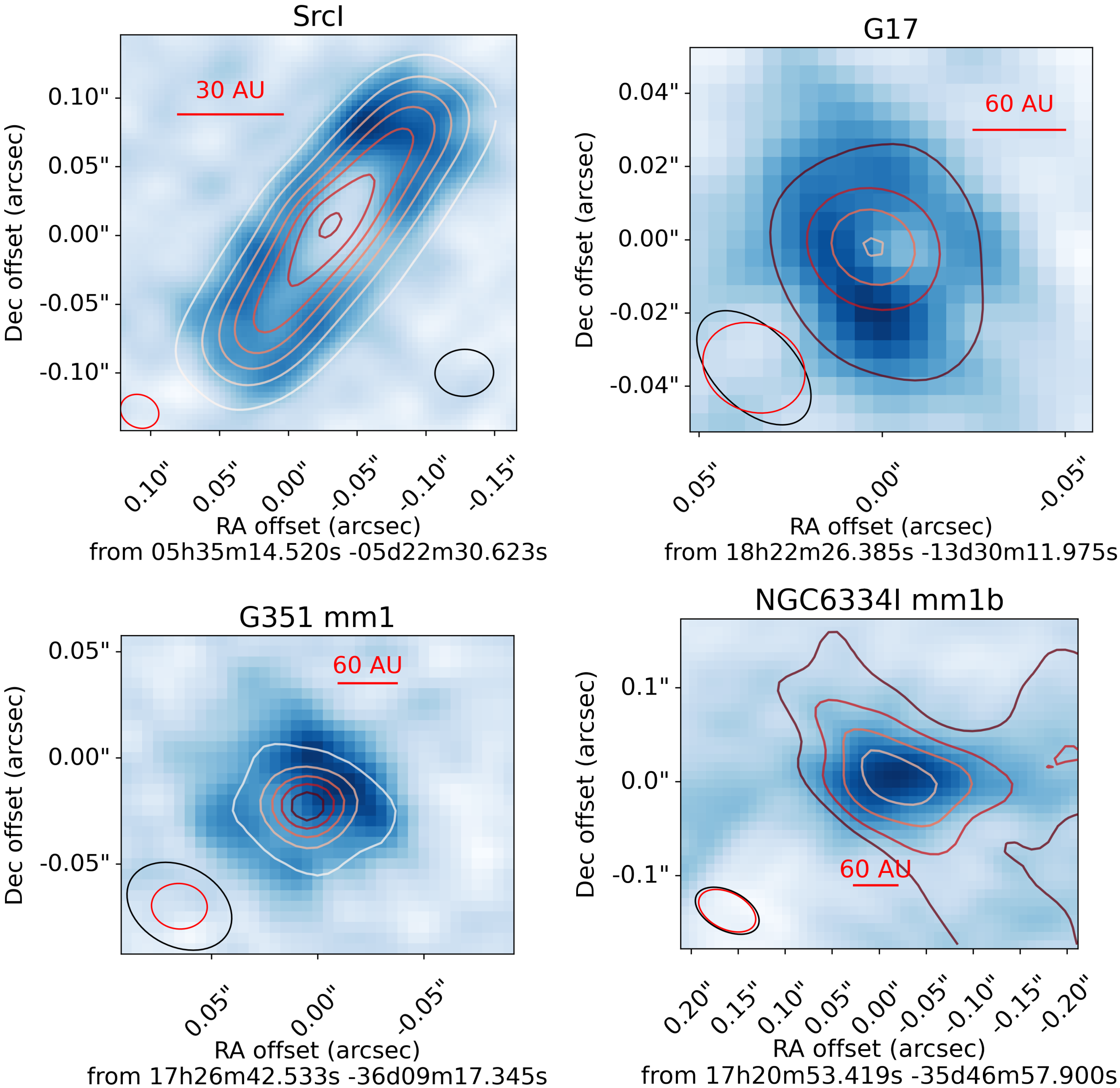

Figure 29. Moment-0 (integrated intensity) images of the resolved sources in NaCl lines as described in Figure 1. The red ellipse shows the continuum beam corresponding to the contours, while the black ellipse shows the line image beam. The contours are: SrcI $\sigma = 0.21$ mJy/beam, contours at 25, 50, 75, 100, 125, 150 σ, G17 $\sigma = 0.12$ mJy/beam, contours at 50, 100, 150, 200 σ, G351mm1 $\sigma = 0.08$ mJy/beam, contours at 50, 75, 100, 125 σ, NGC6334Imm1b $\sigma = 1$ mJy/beam, contours at 10, 15, 20, 25 σ.

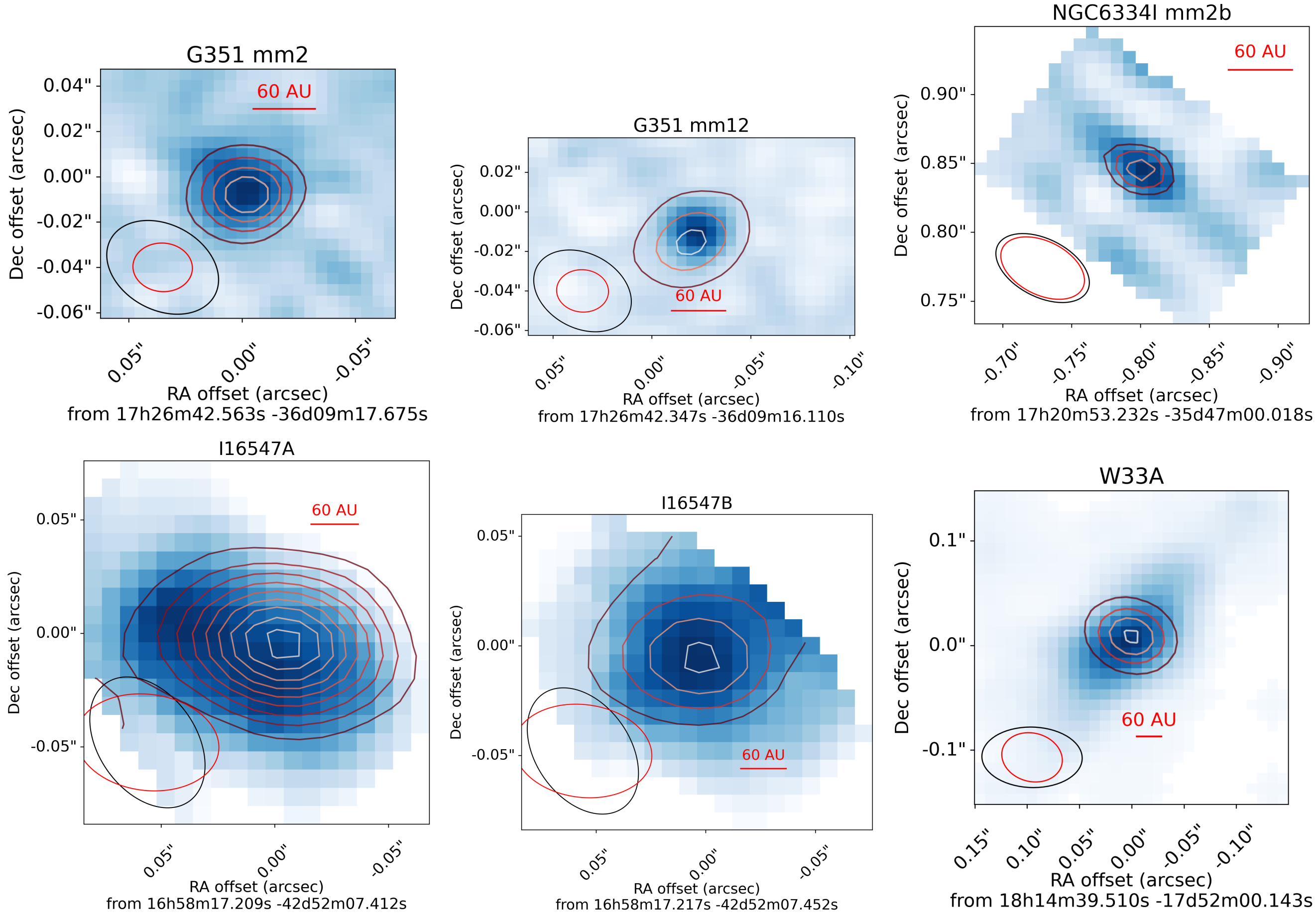

Figure 30. As in Figure 2, but with continuum contours overlaid. The red ellipse shows the continuum beam corresponding to the contours, while the black ellipse shows the line image beam. The contours are: G351mm2 $\sigma = 0.08$ mJy/beam, contours at 50, 75, 100, 125 σ, G351mm12 $\sigma = 0.08$ mJy/beam, contours at 10, 20, 30 σ, NGC6334Imm2 $\sigma = 1$ mJy/beam, contours at 2, 3, 4 σ, I16547A $\sigma = 0.08$ mJy/beam, contours at 100, 150, 200, 250, 300 σ, I16547B $\sigma = 0.08$ mJy/beam, contours at 75, 100, 125, 150 σ, W33A $\sigma = 0.3$ mJy/beam, contours at 20,40,60,80 σ.